The formation of helioseismology lines

I. NLTE effects in alkali spectra

J.H.M.J. Bruls[1], R.J. Rutten[1], and N.G. Shchukina[2]

[1] Sterrekundig Instituut, Postbus 80000, NL–3508 TA Utrecht, The Netherlands
[2] Main Astronomical Observatory, Academy of Sciences of the Ukrainian SSR, 252127 Kiev, USSR

Abstract. We study the NLTE formation of the solar K I and Na I resonance lines employed in helioseismology. We combine standard modeling of the solar atmosphere with comprehensive alkali model atoms, complete up to the Rydberg regime near the continuum, to study various NLTE mechanisms which interact to make the alkali population balances more complex than is the case for other minority species. In particular, we discuss a "photon suction" process which produces overpopulation of the neutral stage by driving a population flow from the reservoir in the singly ionized stage. We isolate this and other mechanisms with specifically tailored model atoms and we provide a choice of simplified model atoms, trading precision against size, which are appropriate for future use in numerical simulations of the solar atmosphere.

Key words: line: formation – Sun: atmosphere – Sun: oscillations – Sun: photosphere

1. Introduction

This is the first paper of a series addressing the formation of solar spectral lines used as Doppler diagnostics in present and future helioseismology: the resonance lines of K I and Na I and the Ni I 676.8 nm line. Our emphasis in these papers lies on departures from local thermodynamic equilibrium (LTE) in the formation of these lines and on effects of the solar granulation on their spatially-averaged emergent line profiles.

This paper investigates NLTE (non–local thermodynamic equilibrium) phenomena in alkali resonance lines, concentrating on the resonance lines of neutral sodium (Na I D_1 at 589.59 nm and Na I D_2 at 589.00 nm, respectively) and the resonance line of neutral potassium at 769.9 nm (the K I 766.5 nm resonance line is severely blended by telluric lines). These alkali lines are important helioseismological diagnostics because their Zeeman splitting and resonant character permit the use of scattering cells to monitor Dopplershifts with high precision and stability. In addition, these lines are employed to measure effects of solar granulation in the middle photosphere and to obtain vector maps of solar magnetic fields.

The main difference between the K I and Na I resonance lines lies in their strength. The K I 769.9 nm line is sufficiently weak that even its line core is fully formed within the solar photosphere; in contrast, the Na I D lines reach line-center optical depth unity in the low chromosphere. Nevertheless, the NLTE formation of these lines is very similar, as are the NLTE mechanisms which affect the overall K I and Na I populations in the solar atmosphere. We therefore treat the two alkali species together in this paper, starting with a brief review of the pertinent literature.

The use of resonance scattering in solar spectrometry was pioneered by Blamont (1953). Blamont & Roddier (1961) used a Sr I resonance spectrometer to measure the gravitational redshift of the sun while Roddier (1965) measured solar line profiles at ultra-high spectral resolution (10^7) with resonance scattering on Ca I, Sr I and Ba I atoms. Fossat & Roddier (1971) were the first to use the Na I D lines in resonance-scattering solar oscillation measurements, starting the French tradition of using sodium cells for whole-disk helioseismology (e.g. Grec et al. 1976, Grec et al. 1983, Robillot et al. 1984); this now culminates in the GOLF experiment to be launched on SOHO (Gabriel et al. 1989). Spatially-resolved sodium-cell helioseismology is achieved with the Cacciani magneto-optical resonance spectrometer (Cacciani & Fofi 1978, Rhodes et al. 1986, 1988); it has also been used to obtain longitudinal magnetograms (Rhodes et al. 1988a) following the original scheme of Cimino et al. (1968). In addition, the Na I D lines are well-known diagnostics of small-scale wave properties in the upper photosphere (e.g. Beckers et al. 1972, Deubner 1974, Cram et al. 1977, Cram 1978, Deubner & Fleck 1989), of sunspot chromospheres (e.g. von Uexküll et al. 1983), and of off-limb chromospheric fine structure (e.g. Gulyaev 1978, 1983).

K I 769.9 nm resonance spectrometry was initialized by Blamont & Chanin (1968) to observe lunar thermoluminescence, while Snider (1970) used it to measure the gravitational redshift at the solar surface (cf. Snider 1972, 1974). Solar oscillation measurements with potassium resonance cells were started by the Birmingham group (Brookes et al. 1978), first at Pic du Midi (Brookes et al. 1976) and later on Tenerife and elsewhere, evolving into extensive helioseismological programs run jointly by the Birmingham and La Laguna groups (e.g. Claverie et al. 1982, Jefferies et al. 1988, Isaak et al. 1989, Pallé et al. 1989a, Pallé et al. 1989b, Elsworth et al. 1990). In addition, the K I 769.9 nm line has been used to measure solar rotation (e.g. Snider 1983, Pierce &

Send offprint requests to: J.H.M.J. Bruls

LoPresto 1984) and to estimate properties of the solar granulation in the middle photosphere. Its limb effect (center-to-limb change in convective line shift) has been measured by Bonet et al. (1989), LoPresto & Pierce (1985) and Andersen et al. (1985). Its spatially-averaged profile and bisector variations have been observed from center to limb for quiet and active regions by Bonet et al. (1988), while Roca-Cortes et al. (1983) have observed its temporal and spatial variations on smaller scales. Finally, Cacciani et al. (1990, 1991) describe a K I version of the magneto-optical filter that produces high-quality vector magnetograms.

Such frequent and varied diagnostic usage of the alkali resonance lines requires understanding of their formation. The existing alkali line formation studies consist of two categories. In the first a standard plane-parallel model of the solar atmosphere is employed to study departures from LTE in "one-dimensional" fashion. For Na I the NLTE groundwork was laid by Johnson (1962), Waddell (1962), Chamaraux (1967), Curtis & Jefferies (1967, summarized in Chapter 9 of Jefferies 1968) and Athay & Canfield (1969); for K I, the pioneering NLTE study was by De la Reza & Müller (1975). These analyses demonstrated that NLTE modeling is required to reproduce the observed cores of the alkali resonance lines because resonance scattering causes their source functions to deviate appreciably from the Planck function. More detailed numerical studies were subsequently reported for Na I by Gehren (1975), Caccin et al. (1980) and Shchukina et al. (1990), for K I by Shchukina (1981), Shchukina & Aleksandrova (1982), McKenna (1984), Severino et al. (1986) and Shchukina (1987).

The second category of alkali line formation studies consists of analyses by the Naples group in which plane-parallel NLTE results are employed to compute K I 769.9 nm line profiles from schematic dynamical models of the granulation and of the photospheric five-minute oscillation (Marmolino et al. 1984, 1987, 1988, Severino et al. 1986, Gomez et al. 1987a, 1991).

This paper re-examines the NLTE properties of the solar K I and Na I spectra adopting one-dimensional modeling; it thus belongs to the first category above. The next paper in this series will follow the Naples example by using results of numerical granulation simulations to reproduce spatially-averaged solar line profiles. Eventually, K I and Na I radiative transfer must be computed self-consistently within detailed multi-dimensional, time-dependent hydrodynamical simulations that fully account for both the solar granulation and the photospheric oscillations. We take a step towards that goal here by concentrating on the NLTE mechanisms which operate in the alkali spectra.

A re-examination of NLTE effects in the solar alkali spectra is warranted at the present time for a number of reasons. First, the availability of new radiative transfer codes, in particular Carlsson's (1986) efficient implementation "MULTI" of the method of Scharmer & Carlsson (1985), renders computations practical without relying on tractability assumptions such as restricted atom size. We employ MULTI to study NLTE effects for comprehensive alkali model atoms, incorporating levels and lines up to the Rydberg regime near the continuum.

Second, MULTI's computational speed also permits the extensive experimentation which is required to understand the results, i.e. to find out not only *how* spectral lines are formed out of LTE but also *why* they are. Such experimentation concerning the details of how the statistical equilibrium is reached within the computational model lacks in much previous work, but it is a prerequisite to diagnostic application and to interpret results from more complex numerical simulations.

Third, although the neutral alkalis possess relatively simple term diagrams, they turn out to display surprisingly complex NLTE properties. In particular, we identify competing NLTE processes which affect the partitioning between the neutral and singly ionized stages and cause the NLTE behavior of the alkalis to be appreciably more complex than for other minority species such as Fe I. The major process is a "photon suction" phenomenon which we demonstrate for K I, but which also operates in other neutral metal spectra such as Mg I in which it produces infrared emission lines (Carlsson et al. 1992).

Indeed, alkali NLTE behavior sets an example for other spectra. The K I ionization energy is only 4.34 eV, the smallest of all abundant species (exceeding only Rb I, Cs I, Fr I and the H⁻ ion); Na I is runner-up at 5.14 eV. The alkali spectra therefore represent prototypes of configurations in which the next ion has nearly all the population, but is well within reach from the neutral stage through both radiative and collisional transitions. Such systems occur higher up in the term diagrams of other neutral species such as Fe I, Mg I, Al I etc., so that alkali NLTE behavior may apply to their highly-excited states as well.

The organization of the paper is as follows. In the next section we discuss modeling assumptions. Section 3 specifies atomic parameters, respectively for K I and for Na I. In Sect. 4 we first analyze the NLTE behavior of K I. We start with a comprehensive model atom and then identify various NLTE mechanisms through experimentation. The same mechanisms apply to Na I, so that it suffices to display results for Na I without duplicating the full analysis. Understanding the mechanisms permits the construction of "confection" model atoms which are appreciably smaller but contain the major K I population and depopulation channels. We end the paper with conclusions in Sect. 5.
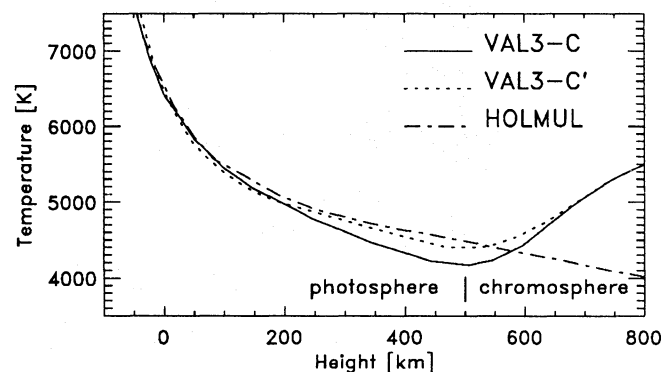

Fig. 1. Temperature stratifications of atmospheric models. Heights measured from optical depth unity at $\lambda = 500$ nm. The temperature minimum is adopted as boundary between photosphere and chromosphere

2. Computational method and atmospheric models

We employ the fast and versatile radiative transfer code MULTI of Carlsson (1986) which is based on the operator perturbation method of Scharmer & Carlsson (1985). We use the version documented by Carlsson (1986) with minor modifications to the opacity package.

Figure 1 shows the temperature stratification of three standard atmospheric models. VAL3-C is the quiet-sun model of Vernazza et al. (1981) and VAL3-C' is its successor as tabulated by Maltby et al. (1986); these one-dimensional Harvard models
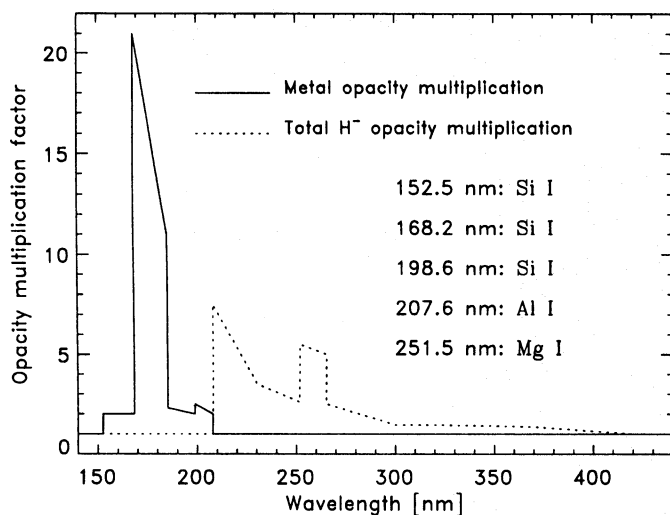
Fig. 2. Opacity multiplication factors as function of wavelength in nm. Solid: applied to MULTI's total metal opacity. Dotted: applied to MULTI's total H⁻ opacity. The larger jumps are at the specified bound-free edges. No opacity enhancement was applied outside this wavelength range
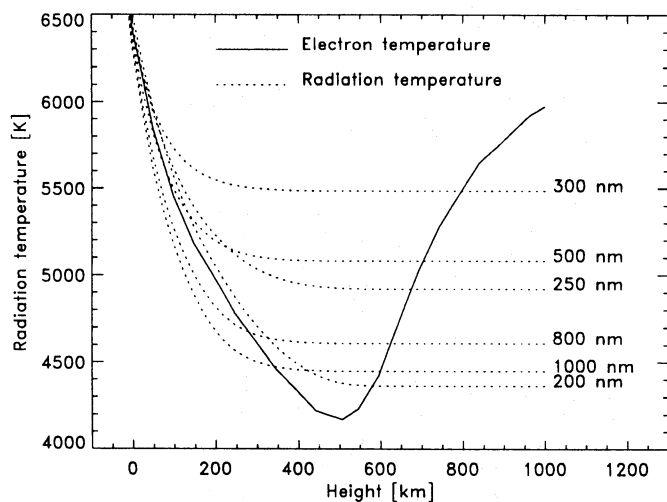

Fig. 3. Dotted: Equivalent black body radiation temperatures at different wavelengths. Solid: VAL3-C electron temperature

differ in having a cool and a hot temperature minimum, respectively. The LTE model of Holweger & Müller (1974), henceforth called HOLMUL, resembles VAL3-C' in the photosphere but does not possess a chromospheric temperature rise. We employ the VAL3-C and HOLMUL models together to cover typical model variations; Fig. 1 shows that their combination duplicates VAL3-C' closely (the chromosphere from VAL3-C, the photosphere from HOLMUL), so that no separate computations are needed for the VAL3-C' model.

We account for radiative damping and Van der Waals damping. The radiative damping widths are taken equal to the sum of the inverse lifetimes τ of the upper and lower levels of each line (Tables 1 and 2), except for the resonance lines for which we specify slightly different values in accordance with the resonance line oscillator strengths (Wiese et al. 1969; Gaupp et al. 1982). Van der Waals damping is evaluated from the classical expression

(Unsöld 1955, p. 332) with the parameter C_6 computed following the angular momentum independent form of the formula by Bates & Damgaard (1949). Stark broadening is negligible for most Na I lines (Gehren 1975); we neglect it for all.

We do not apply ad-hoc damping enhancement factors. Traditionally, such factors are used to increase the collisional damping over the Van der Waals value in order to fit observed spatially-averaged profiles with one-dimensional computations. Sizable enhancements, up to five, have been employed (e.g. Holweger 1971, Holweger & Müller 1974, Evans & Testerman 1975, Gurtovenko & Kondrashova 1980, Gomez et al. 1987b, Gomez et al. 1991), but we discard their use altogether on the suspicion that such excess line broadening stems from atmospheric inhomogeneity rather than from deficiencies in atomic collision theory. We return to this issue in the next paper of this series and accept here that our computed line wings are appreciably narrower than the spatially-averaged profiles observed from the sun. Similar considerations apply to the micro- and macroturbulent broadening parameters, which are also commonly used as fudge parameters to fit observed line cores from one-dimensional modeling. We use the microturbulence specified with each atmospheric model to broaden the line extinction coefficient in most experiments below, but discuss also computations without such microturbulent smearing; we do not apply any macroturbulent smearing to the computed emergent line profiles.

The alkali abundances are taken equal to the values derived by Anders & Grevesse (1989) from the meteoritic alkali/silicon ratios, i.e. $N_K/N_H = 1.35\,10^{-7}$ (5.13 on the $\log N_H = 12$ scale) for potassium and $N_{Na}/N_H = 2.04\,10^{-6}$ (6.31) for sodium.

Various alkali bound-free extinction edges are located in the (near) ultraviolet (Tables 1 and 2). Evaluation of the rates in these edges requires correction for the presence of the host of atomic lines which together make up the ultraviolet "line haze". These are not taken into account in MULTI's standard opacity package which is based on Auer et al. (1972). Since none of these ultraviolet bound-free transitions is very important (see Sect. 3.3), there is no need to specify the line haze in great detail. We therefore apply appropriate frequency-dependent multiplication factors, to the total H⁻ opacity for $\lambda > 208$ nm and to the metal opacity at shorter wavelengths. These factors are shown in Fig. 2 and were determined empirically by fitting the computed VAL3-C continuum intensity to the observed continuum in such a way that the photospheric opacity source with the largest relative contribution is the one that is scaled at each wavelength. The mean continuum radiation fields J_ν that result with this simple recipe are compared with the Planck function B_ν in Fig. 3, in the form of black body radiation temperatures to avoid scale variations with wavelength. They are close to the results of Vernazza et al. (1981) computed with scaled opacity distribution functions following Kurucz (1974).

Finally, partial frequency redistribution of line photons may influence the alkali resonance lines, in particular the Na I D lines which are the stronger ones. Waddell (1962) and Curtis & Jeffries (1967) found empirically that the Na I D line source functions are frequency-independent over much of the line profile. Precise computations have not been carried out so far; we adopt complete redistribution here but evaluate this assumption in a future paper.
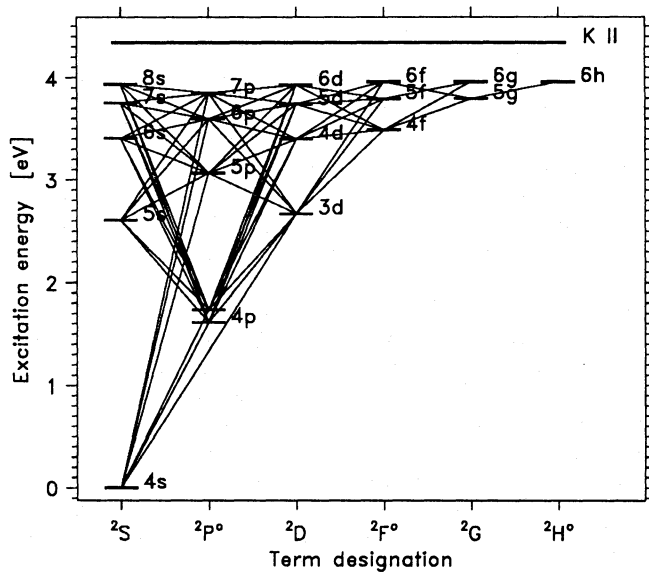
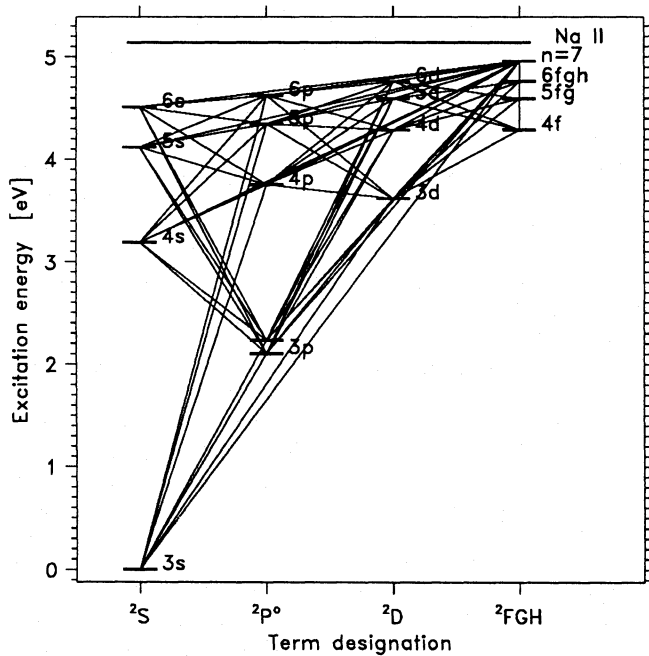**Fig. 4.** Grotrian diagram of the comprehensive K I model atom

Fig. 5. Grotrian diagram of the comprehensive Na I model atom. The excitation energy scaling is the same as for Fig. 4

Table 1. Levels of the K I model atom

Nr	Level	g	τ [ns]	E_{exc} [cm^{-1}]	E_{ion} [eV]	σ_{T} [Mb]
1	$4s\,^2\mathrm{S}^e$	2	∞	0.0	4.339	0.01
2	$4p\,^2\mathrm{P}^o_{1/2}$	2	27.3	12985.2	2.730	6.54
3	$4p\,^2\mathrm{P}^o_{3/2}$	4	27.3	13042.9	2.722	6.67
4	$5s\,^2\mathrm{S}^e$	2	46.4	21026.8	1.733	0.27
5	$3d\,^2\mathrm{D}^e$	10	41.6	21535.4	1.670	28.4
6	$5p\,^2\mathrm{P}^o$	6	133	24713.9	1.276	5.3
7	$4d\,^2\mathrm{D}^e$	10	264	27397.5	0.947	46.7
8	$6s\,^2\mathrm{S}^e$	2	87.8	27450.7	0.934	0.9
9	$4f\,^2\mathrm{F}^o$	14	62.9	28127.9	0.853	36.2
10	$6p\,^2\mathrm{P}^o$	6	310	29004.9	0.744	6.0
11	$5d\,^2\mathrm{D}^e$	10	720	30185.4	0.598	59.1
12	$7s\,^2\mathrm{S}^e$	2	160	30274.3	0.587	1.7
13	$5f\,^2\mathrm{F}^o$	14	114	30606.7	0.546	57.1
14	$5g\,^2\mathrm{G}^e$	18	233	30617.3	0.545	57.1
15	$7p\,^2\mathrm{P}^o$	6	572	31072.9	0.488	7.6
16	$6d\,^2\mathrm{D}^e$	10	1066	31696.0	0.411	66.7
17	$8s\,^2\mathrm{S}^e$	2	269	31765.4	0.402	2.8
18	$6f\,^2\mathrm{F}^o$	14	187	31953.2	0.379	74.3
19	$6g\,^2\mathrm{G}^e$	18	397	31960.0	0.378	74.3
20	$6h\,^2\mathrm{H}^o$	22	397	31962.0	0.378	74.3
21	cont	1	—	35009.8	31.6	—

Table 2. Levels of the Na I model atom

Nr	Level	g	τ [ns]	E_{exc} [cm^{-1}]	E_{ion} [eV]	σ_{T} [Mb]
1	$3s\,^2\mathrm{S}^e$	2	∞	0.0	5.139	0.092
2	$3p\,^2\mathrm{P}^o_{1/2}$	2	16.4	16956.2	3.037	7.95
3	$3p\,^2\mathrm{P}^o_{3/2}$	4	16.4	16973.4	3.035	7.95
4	$4s\,^2\mathrm{S}^e$	2	39.5	25740.0	1.948	0.54
5	$3d\,^2\mathrm{D}^e$	10	19.9	29172.9	1.522	19
6	$4p\,^2\mathrm{P}^o$	6	102	30270.7	1.386	17.5
7	$5s\,^2\mathrm{S}^e$	2	80.3	33200.7	1.023	1.7
8	$4d\,^2\mathrm{D}^e$	10	52.4	34548.7	0.856	35
9	$4f\,^2\mathrm{F}^o$	14	71.6	34586.9	0.851	36
10	$5p\,^2\mathrm{P}^o$	6	342	35042.0	0.794	31
11	$6s\,^2\mathrm{S}^e$	2	152	36372.6	0.630	3.0
12	$5d\,^2\mathrm{D}^e$	10	108	37036.8	0.547	52
13	$5fg\,^2\mathrm{F}^o,^2\mathrm{G}^e$	32	192	37058.7	0.544	57
14	$6p\,^2\mathrm{P}^o$	6	837	37297.2	0.515	44
15	$6d\,^2\mathrm{D}^e$	10	191	38387.3	0.380	70
16	$6fgh\,^2\mathrm{FGH}$	54	329	38400.7	0.378	74
17	$n = 7$	98	604	39146.0	0.286	90
18	cont	1	—	41450.0	47.3	—

3. Atomic data

In this section we specify comprehensive model atoms for K I and Na I. The corresponding Grotrian diagrams are shown in Figs. 4 and 5, respectively. The energy levels are specified in Tables 1 and 2 while the lines are given in Tables 3 and 4 for K I and in Tables 5 and 6 for Na I.

3.1. Energy levels

Our K I model atom is complete up to $n = 6$ and contains $7s\,^2\mathrm{S}^e$, $7p\,^2\mathrm{P}^o$ and $8s\,^2\mathrm{S}^e$ in addition, totalling 20 bound levels and the continuum. We neglect all doublet fine structure except for the

$4p\,^2\mathrm{P}^o$ splitting. The term structure is specified in Table 1. The excitation energies E_{exc} have been taken from Corliss & Sugar (1979) for levels 1 – 18 and 21 and from Park (1971) for levels 19 and 20. Most lifetimes τ are theoretical estimates from Lindgård & Nielsen (1977); the values for level $4p\,^2\mathrm{P}^o$ (Zimmerman 1975) and for $5p\,^2\mathrm{P}^o$ and $6p\,^2\mathrm{P}^o$ (Svanberg 1971) are experimental and in good agreement with the theoretical lifetimes.

The Na I model atom is complete up to $n = 7$; all $n = 7$ states have been "collapsed" into a single level because their similarity makes individual specification unnecessary. A model of 17 bound levels and the continuum results, of similar size as

Table 3. Lines of the K I model atom (part 1)

	Transition	Wavelength nm (air)	f_{lu}
2 – 1	$4s\,^2S^e - 4p\,^2P^o_{1/2}$	769.8970	0.339
3 – 1	$4s\,^2S^e - 4p\,^2P^o_{3/2}$	766.4907	0.682
5 – 1	$4s\,^2S^e - 3d\,^2D^e$	464.2173	$3.6\,10^{-6}$
6 – 1	$4s\,^2S^e - 5p\,^2P^o$	404.5165	$9.1\,10^{-3}$
10 – 1	$4s\,^2S^e - 6p\,^2P^o$	344.6707	$9.0\,10^{-4}$
15 – 1	$4s\,^2S^e - 7p\,^2P^o$	321.7309	$2.14\,10^{-4}$
4 – 2	$4p\,^2P^o_{1/2} - 5s\,^2S^e$	1243.2262	0.183
5 – 2	$4p\,^2P^o_{1/2} - 3d\,^2D^e$	1169.2106	0.90
7 – 2	$4p\,^2P^o_{1/2} - 4d\,^2D^e$	693.6584	$3.7\,10^{-4}$
8 – 2	$4p\,^2P^o_{1/2} - 6s\,^2S^e$	691.1080	$1.960\,10^{-2}$
11 – 2	$4p\,^2P^o_{1/2} - 5d\,^2D^e$	581.2249	$2.9\,10^{-3}$
12 – 2	$4p\,^2P^o_{1/2} - 7s\,^2S^e$	578.2383	$6.2\,10^{-3}$
16 – 2	$4p\,^2P^o_{1/2} - 6d\,^2D^e$	534.3012	$3.4\,10^{-3}$
17 – 2	$4p\,^2P^o_{1/2} - 8s\,^2S^e$	532.3274	$2.68\,10^{-3}$
4 – 3	$4p\,^2P^o_{3/2} - 5s\,^2S^e$	1252.2123	0.183
5 – 3	$4p\,^2P^o_{3/2} - 3d\,^2D^e$	1177.1552	0.90
7 – 3	$4p\,^2P^o_{3/2} - 4d\,^2D^e$	696.4470	$3.77\,10^{-4}$
8 – 3	$4p\,^2P^o_{3/2} - 6s\,^2S^e$	693.8760	$1.96\,10^{-2}$
11 – 3	$4p\,^2P^o_{3/2} - 5d\,^2D^e$	583.1814	$2.77\,10^{-3}$
12 – 3	$4p\,^2P^o_{3/2} - 7s\,^2S^e$	580.1747	$6.2\,10^{-3}$
16 – 3	$4p\,^2P^o_{3/2} - 6d\,^2D^e$	535.9541	$3.33\,10^{-3}$
17 – 3	$4p\,^2P^o_{3/2} - 8s\,^2S^e$	533.9682	$2.69\,10^{-3}$
6 – 4	$5s\,^2S^e - 5p\,^2P^o$	2711.2428	1.5
10 – 4	$5s\,^2S^e - 6p\,^2P^o$	1253.0494	$3.2\,10^{-2}$
15 – 4	$5s\,^2S^e - 7p\,^2P^o$	995.1131	$6.0\,10^{-3}$
6 – 5	$3d\,^2D^e - 5p\,^2P^o$	3145.4885	0.14
9 – 5	$3d\,^2D^e - 4f\,^2F^o$	1516.5176	0.75
10 – 5	$3d\,^2D^e - 6p\,^2P^o$	1338.4479	$6.6\,10^{-3}$
13 – 5	$3d\,^2D^e - 5f\,^2F^o$	1102.0959	0.17
15 – 5	$3d\,^2D^e - 7p\,^2P^o$	1048.2270	$1.9\,10^{-3}$
18 – 5	$3d\,^2D^e - 6f\,^2F^o$	959.6531	$6.8\,10^{-2}$
7 – 6	$5p\,^2P^o - 4d\,^2D^e$	3725.2977	1.2
8 – 6	$5p\,^2P^o - 6s\,^2S^e$	3652.9000	0.32
11 – 6	$5p\,^2P^o - 5d\,^2D^e$	1827.1350	$7.8\,10^{-3}$
12 – 6	$5p\,^2P^o - 7s\,^2S^e$	1797.9428	$2.7\,10^{-2}$
16 – 6	$5p\,^2P^o - 6d\,^2D^e$	1431.8400	$1.5\,10^{-5}$
17 – 6	$5p\,^2P^o - 8s\,^2S^e$	1417.7531	$8.7\,10^{-3}$

Table 4. Lines of the K I model atom (part 2)

	Transition	Wavelength nm (air)	f_{lu}
9 – 7	$4d\,^2D^e - 4f\,^2F^o$	13688.4000	0.372
10 – 7	$4d\,^2D^e - 6p\,^2P^o$	6219.5633	0.311
13 – 7	$4d\,^2D^e - 5f\,^2F^o$	3115.1625	0.412
15 – 7	$4d\,^2D^e - 7p\,^2P^o$	2720.0504	$1.4\,10^{-2}$
18 – 7	$4d\,^2D^e - 6f\,^2F^o$	2194.4680	0.140
10 – 8	$6s\,^2S^e - 6p\,^2P^o$	6432.4059	1.28
15 – 8	$6s\,^2S^e - 7p\,^2P^o$	2759.9906	$5.0\,10^{-2}$
11 – 9	$4f\,^2F^o - 5d\,^2D^e$	4858.7266	$6.0\,10^{-2}$
14 – 9	$4f\,^2F^o - 5g\,^2G^e$	4015.8371	1.35
16 – 9	$4f\,^2F^0 - 6d\,^2D^e$	2801.8096	$8.3\,10^{-3}$
19 – 9	$4f\,^2F^o - 6g\,^2G^e$	2608.7865	0.186
11 – 10	$6p\,^2P^o - 5d\,^2D^e$	8468.3461	1.53
12 – 10	$6p\,^2P^o - 7s\,^2S^e$	7875.6820	0.455
16 – 10	$6p\,^2P^o - 6d\,^2D^e$	3714.9344	$1.6\,10^{-2}$
17 – 10	$6p\,^2P^o - 8s\,^2S^e$	3621.5734	$3.6\,10^{-2}$
13 – 11	$5d\,^2D^e - 5f\,^2F^o$	23730.0391	0.726
15 – 11	$5d\,^2D^e - 7p\,^2P^o$	11265.0172	0.461
18 – 11	$5d\,^2D^e - 6f\,^2F^o$	5655.4238	0.242
15 – 12	$7s\,^2S^e - 7p\,^2P^o$	12518.1383	2.37
16 – 13	$5f\,^2F^o - 6d\,^2D^e$	9177.9977	0.147
19 – 13	$5f\,^2F^o - 6g\,^2G^e$	7387.4914	1.18
18 – 14	$5g\,^2G^e - 6f\,^2F^o$	7483.7625	$8.0\,10^{-3}$
20 – 14	$5g\,^2G^e - 6h\,^2H^o$	7434.6297	1.69
16 – 15	$7p\,^2P^o - 6d\,^2D^e$	16044.5375	1.82
17 – 15	$7p\,^2P^o - 8s\,^2S^e$	14437.1250	0.587

$$f(nL;n'L') = \sum_{JJ'} g(nLJ)f(nLJ;n'L'J') / \sum_{J} g(nLJ) \qquad (1)$$

in which $g(nLJ)$ is the statistical weight of a level with principal quantum number n, total orbital quantum number L and total angular momentum J. The oscillator strength of the forbidden $4s\,^2S^e - 3d\,^2D^e$ line is from Radzig & Smirnov (1985).

Tables 5 and 6 specify all lines used in the comprehensive Na I model. These lists are again complete, with each line a representative transition replacing the actual multiplets. Forbidden transitions are neglected except for $3s\,^2S^e - 3d\,^2D^e$. The oscillator strengths f_{lu} in Table 5 are from Wiese et al. (1969), except for the resonance lines which have been taken from the more recent experiment by Gaupp et al. (1982) whose gf values are 3 – 4% smaller than those of Wiese et al. (1969). The transitions in Table 6 are from Lindgård & Nielsen (1977), who list multiplet values; they agree very well with summations over the component values of Biémont & Grevesse (1973). The oscillator strength of the forbidden $3s\,^2S^e - 3d\,^2D^e$ line is again from Radzig & Smirnov (1985).

3.3. Radiative bound-free transitions

K I photoionization cross-sections have been taken from many sources. We first discuss the $ns\,^2S^e$ transitions which have abnormally small cross-sections due to cancellation effects (e.g. Page 1939, Seaton 1951). The photoionization cross-section from the ground level $4s\,^2S^e$ is relatively well known. Theoretical estimates have been given by e.g. Burgess & Seaton (1960), Moskvin (1963), Fano & Cooper (1968), Weisheit & Dalgarno (1971), Chang & Kelly (1972), Aymar et al. (1976), Hofsaess (1979); experimental results by e.g. Ditchburn et al. (1953), Hudson & Carter (1965),

the K I model. All Na I doublet fine structure is again neglected except for $3p\,^2P^o$. The Na I term structure is specified in Table 2. The excitation energies for levels 1 – 16 and 18 are from Martin & Zalubas (1981), for level 17 from Park (1971). The lifetimes are again theoretical values from Lindgård & Nielsen (1977), except for $4p\,^2P^o$ which is from the experiment by Gaupp et al. (1982).

3.2. Radiative bound-bound transitions

Tables 3 and 4 specify the lines of the comprehensive K I model and contain all permitted transitions; each line is a representative transition that replaces the actual multiplets arising from the level fine structure. Forbidden transitions are neglected except for $4s\,^2S^e - 3d\,^2D^e$. The oscillator strengths f_{lu} in Table 3 are from Wiese et al. (1969) who conveniently specify the required values per multiplet. The oscillator strengths in Table 4 were determined from the component values in Biémont & Grevesse (1973) with the summation rule

Table 5. Lines of the Na I model atom (part 1)

	Transition	Wavelength nm (air)	f_{lu}
2 – 1	$3s\,{}^2S^e - 3p\,{}^2P^o_{1/2}$	589.5921	0.318
3 – 1	$3s\,{}^2S^e - 3p\,{}^2P^o_{3/2}$	588.9948	0.631
5 – 1	$3s\,{}^2S^e - 3d\,{}^2D^e$	342.6861	$6.00\,10^{-3}$
6 – 1	$3s\,{}^2S^e - 4p\,{}^2P^o$	330.2572	$1.42\,10^{-2}$
10 – 1	$3s\,{}^2S^e - 5p\,{}^2P^o$	285.2878	$2.21\,10^{-3}$
14 – 1	$3s\,{}^2S^e - 6p\,{}^2P^o$	268.0372	$7.30\,10^{-4}$
17 – 1	$3s\,{}^2S^e - n = 7$	255.3773	$6.10\,10^{-4}$
4 – 2	$3p\,{}^2P^o_{1/2} - 4s\,{}^2S^e$	1138.1446	0.163
5 – 2	$3p\,{}^2P^o_{1/2} - 3d\,{}^2D^e$	818.3270	0.83
7 – 2	$3p\,{}^2P^o_{1/2} - 5s\,{}^2S^e$	615.4223	$1.37\,10^{-2}$
8 – 2	$3p\,{}^2P^o_{1/2} - 4d\,{}^2D^e$	568.2638	0.106
11 – 2	$3p\,{}^2P^o_{1/2} - 6s\,{}^2S^e$	514.8837	$4.37\,10^{-3}$
12 – 2	$3p\,{}^2P^o_{1/2} - 5d\,{}^2D^e$	497.8543	$3.11\,10^{-2}$
15 – 2	$3p\,{}^2P^o_{1/2} - 6d\,{}^2D^e$	466.4812	$1.40\,10^{-2}$
17 – 2	$3p\,{}^2P^o_{1/2} - n = 7$	450.5306	$9.61\,10^{-3}$
4 – 3	$3p\,{}^2P^o_{3/2} - 4s\,{}^2S^e$	1140.3771	0.163
5 – 3	$3p\,{}^2P^o_{3/2} - 3d\,{}^2D^e$	819.4804	0.833
7 – 3	$3p\,{}^2P^o_{3/2} - 5s\,{}^2S^e$	616.0744	$1.37\,10^{-2}$
8 – 3	$3p\,{}^2P^o_{3/2} - 4d\,{}^2D^e$	568.8197	0.106
11 – 3	$3p\,{}^2P^o_{3/2} - 6s\,{}^2S^e$	515.3401	$4.37\,10^{-3}$
12 – 3	$3p\,{}^2P^o_{3/2} - 5d\,{}^2D^e$	498.2811	$3.11\,10^{-2}$
15 – 3	$3p\,{}^2P^o_{3/2} - 6d\,{}^2D^e$	466.8557	$1.40\,10^{-2}$
17 – 3	$3p\,{}^2P^o_{3/2} - n = 7$	450.8800	$9.67\,10^{-3}$
6 – 4	$4s\,{}^2S^e - 4p\,{}^2P^o$	2206.5463	1.35
10 – 4	$4s\,{}^2S^e - 5p\,{}^2P^o$	1074.7380	$3.85\,10^{-2}$
14 – 4	$4s\,{}^2S^e - 6p\,{}^2P^o$	865.0239	$7.80\,10^{-3}$
17 – 4	$4s\,{}^2S^e - n = 7$	745.7285	$2.84\,10^{-3}$
6 – 5	$3d\,{}^2D^e - 4p\,{}^2P^o$	9106.1563	0.117
9 – 5	$3d\,{}^2D^e - 4f\,{}^2F^o$	1846.5357	1.00
13 – 5	$3d\,{}^2D^e - 5fg\,{}^2FG$	1267.7461	0.159
16 – 5	$3d\,{}^2D^e - 6fgh\,{}^2FGH$	1083.3785	$5.50\,10^{-2}$
8 – 6	$4p\,{}^2P^o - 4d\,{}^2D^e$	2336.8863	0.91
11 – 6	$4p\,{}^2P^o - 6s\,{}^2S^e$	1638.3848	$2.32\,10^{-2}$
12 – 6	$4p\,{}^2P^o - 5d\,{}^2D^e$	1477.5642	0.142
15 – 6	$4p\,{}^2P^o - 6d\,{}^2D^e$	1231.7137	$4.93\,10^{-2}$
17 – 6	$4p\,{}^2P^o - n = 7$	1126.4160	$3.080\,10^{-2}$

Table 6. Lines of the Na I model atom (part 2)

	Transition	Wavelength nm (air)	f_{lu}
10 – 5	$3d\,{}^2D^e - 5p\,{}^2P^o$	1703.3527	$1.631\,10^{-4}$
14 – 5	$3d\,{}^2D^e - 6p\,{}^2P^o$	1230.5345	$3.151\,10^{-5}$
17 – 5	$3d\,{}^2D^e - n = 7$	1002.4182	$2.640\,10^{-2}$
7 – 6	$4p\,{}^2P^o - 5s\,{}^2S^e$	3412.0871	0.311
10 – 7	$5s\,{}^2S^e - 5p\,{}^2P^o$	5429.3043	1.875
14 – 7	$5s\,{}^2S^e - 6p\,{}^2P^o$	2440.4357	$6.180\,10^{-2}$
17 – 7	$5s\,{}^2S^e - n = 7$	1681.5342	$1.378\,10^{-2}$
10 – 8	$4d\,{}^2D^e - 5p\,{}^2P^o$	20266.8609	0.229
13 – 8	$4d\,{}^2D^e - 5fg\,{}^2FG$	3983.0277	0.8594
14 – 8	$4d\,{}^2D^e - 6p\,{}^2P^o$	3637.4375	$8.505\,10^{-4}$
16 – 8	$4d\,{}^2D^e - 6fgh\,{}^2FGH$	2595.3672	0.1851
17 – 8	$4d\,{}^2D^e - n = 7$	2174.6182	$7.26\,10^{-2}$
12 – 9	$4f\,{}^2F^o - 5d\,{}^2D^e$	4080.7910	$1.037\,10^{-2}$
13 – 9	$4f\,{}^2F^o - 5fg\,{}^2FG$	4044.5484	1.343
15 – 9	$4f\,{}^2F^o - 6d\,{}^2D^e$	2630.6254	$1.829\,10^{-3}$
16 – 9	$4f\,{}^2F^o - 6fgh\,{}^2FGH$	2621.3470	0.1828
17 – 9	$4f\,{}^2F^o - n = 7$	2192.8287	$5.92\,10^{-2}$
11 – 10	$5p\,{}^2P^o - 6s\,{}^2S^e$	7513.3977	0.4519
12 – 10	$5p\,{}^2P^o - 5d\,{}^2D^e$	5011.8336	1.055
15 – 10	$5p\,{}^2P^o - 6d\,{}^2D^e$	2988.5096	0.1726
17 – 10	$5p\,{}^2P^o - n = 7$	2435.9988	$9.40\,10^{-2}$
14 – 11	$6s\,{}^2S^e - 6p\,{}^2P^o$	10812.9656	2.305
17 – 11	$6s\,{}^2S^e - n = 7$	3604.7262	$8.610\,10^{-2}$
16 – 12	$5d\,{}^2D^e - 6fgh\,{}^2FGH$	7329.6352	0.8039
17 – 12	$5d\,{}^2D^e - n = 7$	4739.7555	0.195
15 – 13	$5fg\,{}^2FG - 6d\,{}^2D^e$	7524.9469	$1.17\,10^{-2}$
16 – 13	$5fg\,{}^2FG - 6fgh\,{}^2FGH$	7449.5336	1.181
17 – 13	$5fg\,{}^2FG - n = 7$	4789.6047	0.234
15 – 14	$6p\,{}^2P^o - 6d\,{}^2D^e$	9171.1336	1.164
17 – 14	$6p\,{}^2P^o - n = 7$	5407.3938	0.787
17 – 15	$6d\,{}^2D^e - n = 7$	13176.2375	1.156
17 – 16	$6fgh\,{}^2FGH - n = 7$	13414.0109	1.591

Hudson & Carter (1967b), Marr & Creek (1968) and Sandner et al. (1981). The $4s\,{}^2S^e$ cross-section at threshold is 10 – 100 times smaller than a hydrogenic model would predict and ranges over a factor of 4 between different authors; the value of 0.01 Mb in Table 1 is from Hudson & Carter (1965). The shape of the cross-section away from threshold is also non-hydrogenic; it has a minimum near 0.2 eV from threshold and rises to large values for larger energy separation. We use the table given by Mathisen (1984) which is based on Hudson & Carter (1965, 1967b). The other excited levels of the $ns\,{}^2S^e$ series have similar non-hydrogenic properties, with very small cross-sections at threshold and deep minima at larger energy separations. The values at threshold in Table 1 are taken from Fig. 1 of Aymar et al. (1976); we adopt hydrogenic v^{-3} decay for the higher $ns\,{}^2S^e$ levels. Their cross-sections are sufficiently small that they do not influence the K I ionization balance noticeably; detailed specification of their frequency dependence is therefore not required.

We now turn to the other series. The computations by Aymar et al. (1976) and Hofsaess (1979) show that also the $np\,{}^2P^o$ levels have non-hydrogenic character. The cross-sections at threshold are much larger than for the $ns\,{}^2S^e$ series, but they are still smaller and increase much slower with n than hydrogenic transitions. The frequency dependences of the $np\,{}^2P^o$ cross-sections do not display minima. The $4p\,{}^2P^o$ and $5p\,{}^2P^o$ cross-sections even have maxima away from threshold; further out, their decrease with frequency is much slower than v^{-3}. Since these two levels are very important in the ionization equilibrium, their frequency dependence must be entered in detail. We adopt the cross-sections given by Hofsaess (1979). His threshold cross-sections are very close to the ones of Aymar et al. (1976) and he conveniently tabulates the frequency dependence. The cross-sections of the higher $np\,{}^2P^o$ levels also have non-hydrogenic shapes, but they are less important for the ionization balance; a test comparing results from Hofsaess' values with hydrogenic v^{-3} decay shows that the latter is a sufficiently accurate approximation. For the $nd\,{}^2D^e$ series the computations of Aymar et al. (1976) show that the cross-sections are of the same order as hydrogenic values at threshold, and therefore much larger again than $np\,{}^2P^o$ cross-sections. The values in Table 1 are taken from their Fig. 3 and their decay with frequency is again taken to be hydrogenic.

Finally, for the $nf\,{}^2F^o$, $ng\,{}^2G^e$ and $nh\,{}^2H^o$ series we use truly hydrogenic values. To ensure homogeneity in our input data, we

adopt the values plotted for the nd series of hydrogen itself in Fig. 3 of Aymar et al. (1976) rather then using the usual Kramers formula which averages over all l values.

Let us now turn to Na I. It has similar photoionization properties as K I; many sources in the literature cover both spectra together. The $ns\,^2S^e$ transitions again have small cross-sections due to cancellation effects (e.g. Page 1939, Seaton 1951), but these are not as extreme as for K I. Theoretical estimates for the ground level $3s\,^2S^e$ photoionization cross-section have been given by e.g. Aymar (1978), Laughlin (1978), Aymar et al. (1976), Hofsaess (1979) and Butler & Mendoza (1983), while experimental results are available from Ditchburn et al. (1953), Hudson & Carter (1967a), Marr & Creek (1968) and Sandner et al. (1981). The $3s\,^2S^e$ ionization cross-section is very small, and the values of the different authors range over a factor of 2. The shape of the cross-section away from threshold is also non-hydrogenic; it displays a wide "Cooper" minimum near 1.2 eV from threshold and then rises again to large values for larger energy separation. We use the table given by Mathisen (1984) which is based on Hudson & Carter (1967a) and Butler & Mendoza (1983).

The photoionization cross-sections of the excited levels of the $ns\,^2S^e$ series have similar non-hydrogenic properties, but again they are sufficiently small that they are not important in the ionization equilibrium, so that detailed specification of their frequency dependence is not required. The values at threshold in Table 2 are taken from Fig. 1 of Aymar et al. (1976); we adopt hydrogenic v^{-3} decay.

Just as for K I, the Na I $np\,^2P^o$ levels have non-hydrogenic character especially away from threshold (Aymar et al. 1976). The cross-sections at threshold are again much larger than for the $ns\,^2S^e$ series, although still up to 30% smaller than hydrogenic. However, they increase about hydrogenically with n, their frequency dependencies have no minima and are close to hydrogenic decay. We adopt the latter for all $np\,^2P^o$ levels. The values at threshold are taken from Aymar et al. (1976), except for $3p\,^2P^o$ for which we use the value of Mathisen (1984) which is based on Rothe (1969) as rescaled by Laughlin (1978), and which is about 10% larger than the one by Aymar et al. (1976).

The $nd\,^2D^e$ series cross-sections in Table 2 are again from Fig. 3 of Aymar et al. (1976), with hydrogenic decay; for the $nf\,^2F^o$, $ng\,^2G^e$ and $nh\,^2H^o$ (part of level $n = 7$) levels we also use these H I nd values.

3.4. Collisional bound-bound transitions

The neutral alkalis share the usual problem of astrophysical spectrometry that reliable collision cross-sections are scarce. Fortunately, they do not share the usual problem that even unreliable values are hard to find, being scattered throughout the physics literature, because Park (1971) has provided a useful compilation of bound-bound electron collision rates for the alkalis. It is based on various theoretical estimates and measurements and serves as a relatively homogeneous and complete source of K I and Na I electron collision data. Park used the Born approximation as specified in the tables of Vainstein & Sobelman (1968) for transitions between levels with effective quantum number $0.5 \le n_{\text{eff}} \le 5$ and angular quantum number $l \le 2$; his values for $n_{\text{eff}} \ll 5$ transitions are based on the Born-Bethe approximation as given by Omidvar (1969). Both approximations are based on the assumption that the high levels in K I are hydrogenic; they are valid only if the kinetic energy of the incident electron exceeds the difference in excitation energy between the two levels (Bely

& van Regemorter 1970), and would produce large overestimates for transitions between levels close in energy, in particular the $\Delta n = 1$ transitions. For the latter Park applied the semi-classical impact parameter method of Saraph (1964), which is estimated to give 50% precision (Bely & van Regemorter 1970). Finally, Park applied suitable correction factors obtained from experimental data; he estimates the resulting accuracy to be generally within a factor of 2.

Not all of our K I and Na I levels coincide with Park's, requiring some manipulation of his results. Park uses the following formula for the excitation rate from level i to level j

$$C_{ij} = \frac{g_j C(ij)\left(T/10^4\right)^{r(ij)}}{n_i^5 n_j^5 \left(1/n_i^2 - 1/n_j^2\right)^4} \exp\left(-\frac{E_j - E_i}{kT}\right) N_e, \qquad (2)$$

supplying tables of the coefficients $C(ij)$ and $r(ij)$; these permit appropriate scaling of rates for the following differences between Park's level designations and ours.

First, Park does not split any doublet, as we must for K I $4p\,^2P^o$ and Na I $3p\,^2P^o$ in order to separate the resonance lines. For the fine-structure transitions ($4p^2P^o_{1/2} - 4p^2P^o_{3/2}$ and $3p^2P^o_{1/2} - 3p\,^2P^o_{3/2}$, respectively) we apply unity collision strength Ω for lack of suitable data. Note that such a small value of Ω already produces nearly detailed balance in this transition; its precise value is therefore unimportant. For the resonance transitions we apply Park's combined value for each; this may overestimate the electron collision rate in at least one of them, but probably by no more than the intrinsic uncertainty in Park's coefficients. For upward transitions out of the split K I $4p\,^2P^0$ and Na I $3p\,^2P^o$ levels we similarly apply Park's combined rate coefficients.

Second, for K I we include levels $7s\,^2S^e$ and $7p\,^2P^o$ separately whereas Park groups all $n = 7$ levels into a single one; in addition, our K I model atom includes the $8s\,^2S^e$ level. This problem does not arise for our Na I model atom because it combines levels in the same manner as Park did. For the K I transitions with $7s$, $7p$ or $8s$ as upper level we split Park's values by assuming (i)—that the collision rates from level i to level $7s$ equal those from level i to level $7p$, (ii)—that the total collision rate from level i to all $n = 7$ levels equals the sum of the rates to $7s$ and $7p$, and (iii)—that the temperature-dependence of the collision rates is approximately the same for both upper levels. The tables of Kunc & Zgorzelski (1977) show that (i) and (ii) are valid assumptions to within a factor of 2, while (iii) can be verified from Park's Table 5e for levels with $n = 6$.

For upward transitions out of the K I $7s\,^2S^e$ and $7p\,^2P^o$ levels we cannot simply apply Park's combined coefficients because $7s$ and $7p$ have different excitation properties; we therefore scale the C-coefficient of similar transitions lower down in the term diagram with a formula derived from the Born approximation (Sobelman et al. 1981, Eq. 6.1.14):

$$C(ij) = C(pq)\frac{g_q}{g_j}\frac{n_p^3 n_q^3}{n_i^3 n_j^3}\frac{\left(n_j^2 - n_i^2\right)^4}{\left(n_q^2 - n_p^2\right)^4}\frac{\Delta E_{pq}}{\Delta E_{ij}}\left(\frac{E_j^{\text{ion}} E_p^{\text{ion}}}{E_i^{\text{ion}} E_q^{\text{ion}}}\right)^{3/2} \qquad (3)$$

where ij is the transition for which $C(ij)$ is sought and pq is the lower-lying similar transition. For upward transitions out of $8s\,^2S^e$ we apply unit collision strength $\Omega = 1$.

Finally, there are some transitions in the upper part of the comprehensive atoms for which Park's estimates and our scalings are overly large because the energy separations between the lower and upper levels are very small. These are the transitions $7s - 5f$, $7s - 5g$, $5g - 7p$, $7p - 6d$, $6d - 8s$, $8s - 6f$, $6f - 6g$ and $6g - 6h$ in K I and $4d - 4f$, $5d - 5fg$ and $6d - 6fgh$ in Na I for which

we replace Park's values by setting the collision strength Ω to unity. This value is probably too small for most transitions, but the choice already produces collisional domination in this part of the atom, so that there is no need to estimate Ω with more precision.

Similarly, there is no need to specify collision rates for encounters with neutral hydrogen atoms (cf. Steenbock & Holweger 1984) which are probably sizable for "l-changing" quasi-elastic collisions between close Rydberg levels with the same values of n (Omont 1977, cf. Carlsson et al. 1992), just as they are important for elastic collision broadening. However, these also apply to levels that are already collisionally coupled by electron collisions alone.

Table 7. K I ground-level bound-free rates per unit electron density. Numbers in first column refer to reference numbers in text

Ref.	Temperature (K)				
	4000	5000	6000	7000	8000
1	7.98(-14)	1.19(-12)	7.44(-12)	2.98(-11)	7.65(-11)
2	1.26(-13)	1.74(-12)	1.02(-11)	3.57(-11)	9.63(-11)
3	3.20(-13)	4.44(-12)	2.60(-11)	9.33(-11)	2.45(-10)
4	1.42(-13)	2.05(-12)	1.25(-11)	4.62(-11)	1.25(-10)
5	1.87(-13)	2.77(-12)	1.70(-11)	6.32(-11)	1.70(-10)

3.5. Collisional bound-free transitions

Bound-free collision rates have been computed for the alkalis by Kunc & Zgorzelski (1977) [1] from a classical binary encounter theory. For the ionization out of the ground level a comparison can be made with the empirical approximations given by Allen (1976) [2], Lotz (1966, 1967, 1968) [3], Drawin & Emard (1977) [4] and the theoretical approximation given in Eq. (6.1.27) and Table 6.11 of Sobelman et al. (1981) [5] which is based on the Born approximation. Results for K I are given in Table 7.

In general, bound-free collision cross-sections and rates have smaller errors than is the case for bound-bound transitions (Bely & van Regemorter 1970), but Table 7 displays differences up to a factor of 4 between different sources for the K I ground level cross-section. Unfortunately, only the data of Kunc & Zgorzelski (1977) and Allen's formula are applicable for other levels than the ground level. Since Allen's formula is a very general approximation, we use the alkali-specific tables by Kunc & Zgorzelski (1977) in our comprehensive model atoms, but for our experiments with smaller model atoms in section 4.2 we employ Allen's recipe. Note, however, that the 30% difference between Allen (1976) and Kunc & Zgorzelski (1977) changes the resulting populations by less than 1.5% and the ratios of individual level populations by less than 0.3%.

4. Results

In this section we first present results for the comprehensive K I and Na I model atoms. These model atoms were established after many numerical experiments; below, we display some of this experimentation to illustrate basic alkali NLTE processes and their sensitivity to atomic parameter choices. We identify the NLTE processes only for K I because they operate very similarly in Na I; at the end of the section we discuss the overall NLTE behavior for K I and Na I separately.
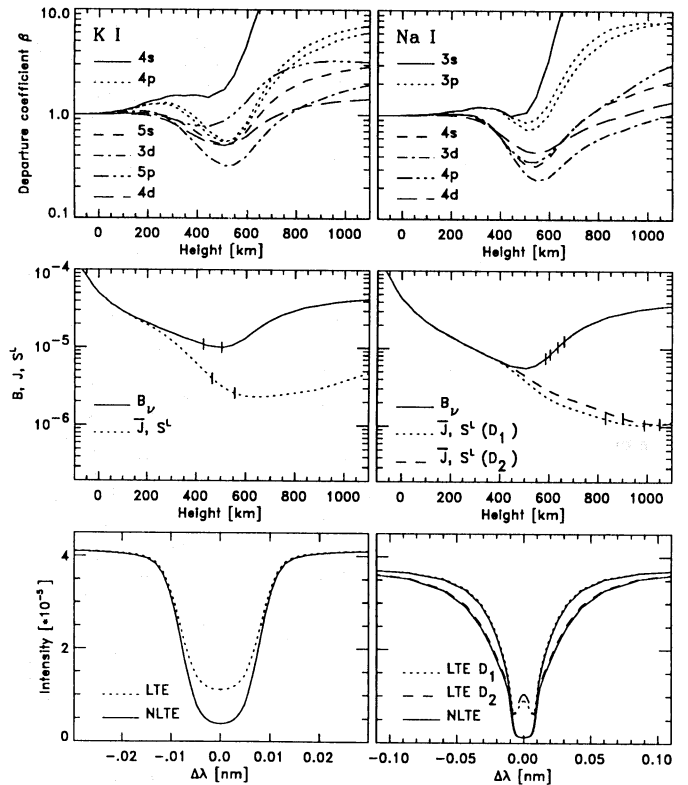

Fig. 6. VAL3-C results for comprehensive K I model (left column) and comprehensive Na I model (right column). Top row: departure coefficients; only lower-level β's are plotted for clarity. Middle row: resonance line source functions S^L, Planck functions $B_\nu(T_e)$ and line-averaged radiation fields $\bar{J}$; $\bar{J}$ and S^L coincide for all three lines (one K I line, left; two Na I D lines, right). Tickmarks indicate locations of total optical depth at line center $\tau = 0.2$ and $\tau = 1$ for the three lines (on S^L curves for NLTE line formation, on B_ν curves for LTE line formation). Bottom row: LTE (dotted, dashed) and NLTE (solid) resonance line profiles. Deviations from LTE occur only in the line cores. Units of B_ν, S^L, $\bar{J}$ and I_ν: erg cm^{-2} s^{-1} Hz^{-1} sr^{-1}

4.1. Comprehensive model atoms

Figures 6 and 7 display population departure coefficients, resonance line source functions, angle-averaged radiation fields and line profiles for the VAL3-C and HOLMUL atmospheric models, respectively. Each figure contains results for K I (left) and Na I (right) to illustrate the large similarity of their behavior. Note that we display results for both Na I D lines, but for only one K I resonance line because the other is severely blended.

The top panels of Figs. 6 and 7 show population departure coefficients defined as $\beta = n^{\mathrm{NLTE}}/n^{\mathrm{LTE}}$, where the LTE population n^{LTE} is related to the total potassium or sodium population of all levels and ionization stages through the Saha and Boltzmann equations following Wijbenga & Zwaan (1972). The ratio β_u/β_l of the upper and lower level departure coefficients of a spectral line sets the departure of its source function from the Planck function; the line opacity scales approximately with the lower-level departure coefficient β_l, exactly so when stimulated emission is negligible.

These population departures show patterns which we explain in more detail below; roughly, they consist of outward divergence between the curves for different levels, with dips and
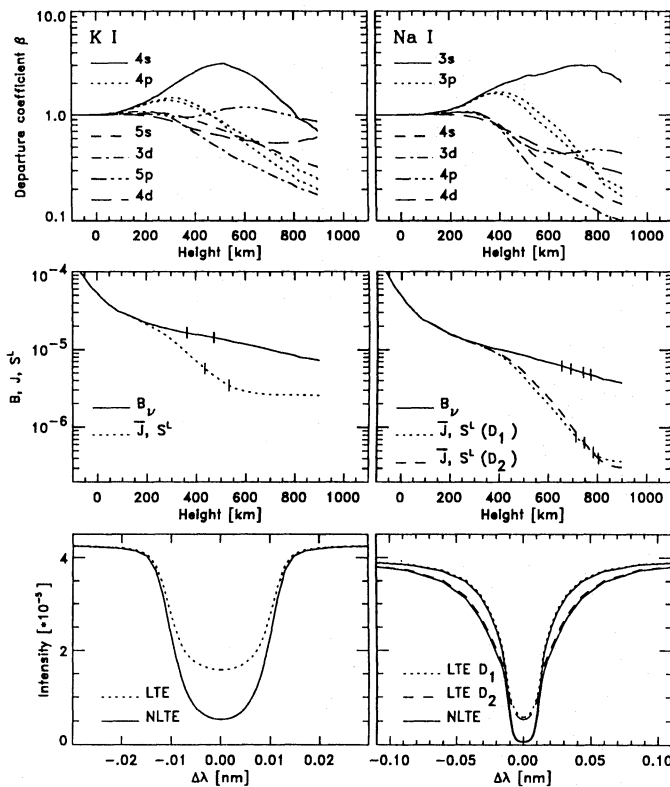
Fig. 7. HOLMUL results for comprehensive atoms. Left: K I; right: Na I. Coding as for Fig. 6

chromospheric upturns for the VAL3-C model and humps and chromospheric downturns for the HOLMUL model. The curve divergences are due to photon losses in lines. They are largest between the resonance-line coefficients (β_{4s} and the β_{4p} pair of K I; β_{3s} and the β_{3p} pair of Na I); these go together with a peculiar photospheric overpopulation of the 4s and 3s ground states, most outspoken for K I and the HOLMUL model, to which we return below.

With increasing height, the departure coefficients in Fig. 6 first display a dip in the temperature minimum region and then a rise in the chromosphere. This pattern corresponds to the temperature stratification of the VAL3-C model in the sense that it portrays differences between the electron temperature and the radiation temperatures which characterize violet and ultraviolet ionizing radiation fields. The pattern is not particular to the alkalis; the classic example was given for Fe I in the analyses of Athay & Lites (1972) and Lites (1972) and it is common to all minority species with well-populated levels about 2 – 4 eV from the continuum. Radiative overionization out of such levels occurs wherever the angle-averaged intensity J_ν exceeds the Planck function $B_\nu(T_e)$ in the 200 – 500 nm wavelength region; for the VAL3-C atmosphere and other models with a cool temperature minimum, such superthermal radiation is present in the temperature minimum region. The initial drop of the HOLMUL temperature is less steep (Fig. 1), which is reflected by the smaller initial drop of the higher-level departure coefficients in the top panels of Fig. 7.

The chromospheric behavior of the departure coefficients originates in similar fashion. The ionization balance is dominated in the chromosphere by irradiation from below, with con-

stant radiation fields; the departure coefficients therefore simply reflect the variation of the LTE reference populations in this regime. The chromospheric temperature rise of the VAL3-C atmosphere (Fig. 6) results in small LTE populations, increasingly smaller than the actual populations, and therefore in NLTE departure coefficients far above unity; for the HOLMUL model, the mapping results in outward decline of the departure coefficients (Fig. 7) because the electron temperature of this model falls deeper and deeper below the ionizing radiation temperatures.

The middle panels of Figs. 6 and 7 show Planck functions $B_\nu(T_e)$, NLTE line source functions S^L and mean radiation fields $\bar{J}$ for the resonance lines; the latter are averaged both over angle and over the line profile. The tick marks on the $B_\nu(T_e)$ and S^L curves indicate line-center formation height; they specify the locations where the total monochromatic optical depth at line center reaches $\tau_\nu = 0.2$ and $\tau_\nu = 1$, for LTE and NLTE modeling respectively. The lines are formed further outward in the NLTE case than for LTE due to the larger NLTE line opacity. The shift is especially large for Na I and the VAL3-C model because the VAL3-C chromosphere contributes noticeable opacity to the Na I D lines, much more than when the ionization balance would follow the Saha equation.

The NLTE line source functions S^L diverge from the local Planck functions $B_\nu(T_e)$ already far below line optical depth unity, reflecting the corresponding departure coefficient divergence in the top panels; this behavior is due to resonance scattering to which we return below. The divergence starts deeper in the photosphere for K I 769.9 nm than for the Na I D lines because the potassium abundance is lower than the sodium abundance; the same ratio sets the difference in LTE formation height.

The bottom panels show emergent disk-center line profiles for the three resonance lines. These are the only line profiles shown in this paper; our subsequent figures display profile changes differentially to these. We make no comparison with observed profiles here because such comparisons are the topic of our next paper in this series. (The wings of the computed profiles shown here fit badly since we do not apply any ad-hoc damping enhancement.) The profiles show the familiar NLTE deepening that results from the S^l/B_ν drop below unity, displayed as divergence between S^L and B_ν in the middle panels and as divergence between β_u and β_l in the top panels. The two LTE Na I D profiles display unrealistic chromospheric reversals. Toward the far wings, LTE becomes a valid description in all plots.

4.2. NLTE processes in K I

Several NLTE mechanisms interact in the solar alkali spectra to produce surprisingly complex behavior. The major ones are:

- resonance line scattering and photon loss;
- photon suction;
- ultraviolet overionization;
- (infra)red overrecombination;
- ultraviolet line pumping.

In this section we discuss numerical experiments for K I that serve to disentangle these processes and to establish their importance, using specially tailored model atoms of different size. Note that full didactic separation into component processes is not possible, since all processes interact in complex ways to establish statistical equilibrium for every model atom employed; in particular, it is often hard to determine which net rates are driving others and which net rates are driven by others. Nevertheless, we find that tailored-atom experimentation is a valuable tool to gain

246

understanding of how statistical equilibrium is reached. As noted above, we display these experiments only for K I, because the same mechanisms operate very similarly in Na I.
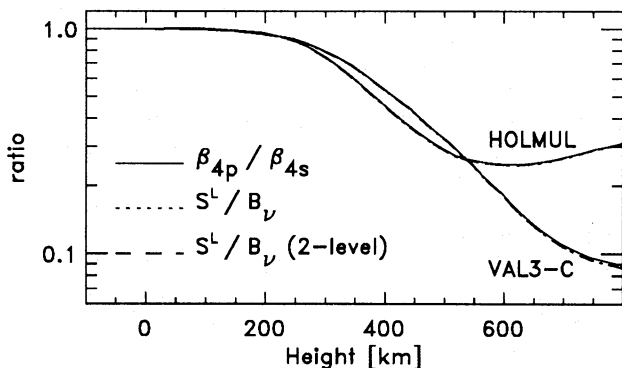

Fig. 8. K I ratios of departure coefficients β_{4p}/β_{4s} (solid), ratios of line source functions to Planck functions S^L/B_ν (dotted) and ratios of equivalent 2-level line source functions to Planck functions (dashed), respectively for VAL3-C and HOLMUL. The three curves in each set virtually coincide; the VAL3-C and HOLMUL results are nearly equal in the photosphere
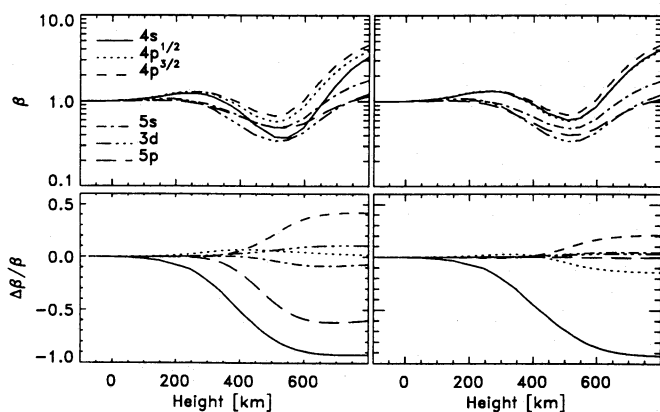
Fig. 9. K I results as function of height for a model atom without resonance lines, using the VAL3-C atmosphere. Top: departure coefficients. Bottom: change of departure coefficients relative to comprehensive-atom results. Left: including the $4s - 5p$ pumping transition. Right: without the $4s - 5p$ pumping transition. Only the lower 6 levels are plotted for clarity

4.2.1. Resonance line scattering and photon loss

Resonance line scattering and photon loss manifest themselves as the deeply-located divergence of the K I $4s$ and $4p$ departure coefficients in Figs. 6 and 7. This deep split, well below the location of line optical depth τ^L_ν unity, results from surface losses near $\tau^L_\nu = 1$ which are propagated by scattering to far below that surface, to line-center optical depth $\tau^L_{\nu_0} \approx 30$ which corresponds to continuum optical depth $\tau^c_\nu = 0.1$. The divergence is controlled by the amount of collisional thermalization, which destroys scattering photons on their way out, and is measured by the departure coefficient ratio $\beta_u/\beta_l = \beta_{4p}/\beta_{4s}$. This ratio corresponds directly to the ratio of the line source function to the Planck function

$$\frac{S^L}{B_\nu(T)} = \frac{\beta_{4p}}{\beta_{4s}} \frac{1 - e^{-h\nu/kT}}{1 - (\beta_{4p}/\beta_{4s})e^{-h\nu/kT}} \approx \frac{\beta_{4p}}{\beta_{4s}} \qquad (4)$$

because the correction for NLTE stimulated emission amounts to only a few percent; the corresponding curves in Fig. 8 therefore coincide. They also coincide with the curves specifying the ratio of the equivalent two-level line source function to the Planck function, given by

$$\frac{S^L}{B_\nu(T_e)} = \frac{(1-\epsilon)\bar{J} + \epsilon B_\nu(T_e)}{B_\nu(T_e)}, \qquad (5)$$

where we use the computed line photon destruction probability

$$\epsilon = C_{ul}/(A_{ul} + B_{ul}\bar{J} + C_{ul}). \qquad (6)$$

This coincidence demonstrates that the K I resonance line source function is described accurately by the two-level approximation, i.e. that the indirect photon destruction processes specified by the $\eta B_\nu(T^*)$ term in the formal expression

$$S^L = (1-\epsilon)\bar{J} + \epsilon B_\nu(T_e) + \eta B_\nu(T^*) \qquad (7)$$

are negligible.

The two sets of curves in Fig. 8 for the VAL3-C and HOLMUL models, respectively, do not differ in the photosphere because the two models are similar there, the main difference being a shift of the $\tau^L_{\nu_0} = 1$ location which lies 40 km deeper in the HOLMUL atmosphere. At larger height, the absence of a chromospheric temperature rise in the HOLMUL model results in smaller NLTE divergence. In fact, this model was constructed to fit strong optical Fe I lines, with a temperature decay set to mimic typical NLTE Fe I behavior rather than the true electron temperature (Holweger 1967, cf. Rutten & Kostik 1982); the deviation from unity shown by the HOLMUL curves in Fig. 8 demonstrates that scattering is more important in the K I resonance lines than in the strong optical Fe I lines.

The two-level character of the K I resonance lines is enhanced by the very weak coupling between the $4s$ ground state and the continuum. The collisional coupling is small because the 4.34 eV energy separation is too large to be bridged by thermal collisions; the radiative coupling is small because the $4s$ photoionization cross-section is exceptionally small. Thus, the resonance lines dominate the behavior of the $4s$ population relative to $4p$, nearly without interference from processes occurring in other parts of the K I Grotrian diagram. We demonstrate this with Fig. 9. The upper panels show the departure coefficients that result when the resonance doublet is taken out of the comprehensive model atom; the lower panels show their changes relative to the comprehensive results, negative values implying downward shifts of the β curves in Fig. 6. The largest change occurs indeed for the $4s$ ground state.

Omission of the resonance lines affects the higher levels as well (left-hand panels), but this is caused by the secondary coupling between the ground state and higher levels through the optical $4s - 5p$ transition. This is a pumping transition discussed below; it communicates the drop in the $4s$ population via $5p$ to the higher part of the Grotrian diagram. The right panels of Fig. 9 shows results when also this pumping line is omitted; omission of the resonance lines then affects only the ground state population.

4.2.2. Photon suction

We now turn to the NLTE photon suction process which produces the appreciable overpopulation of the $4s$ ground state seen in Figs. 6 and 7. Although the divergence between the $4s$ and $4p$ population departures is fully set by resonance line photon losses, this does not explain why the ground state is overpopulated in the photosphere and even in the temperature minimum. In fact, this
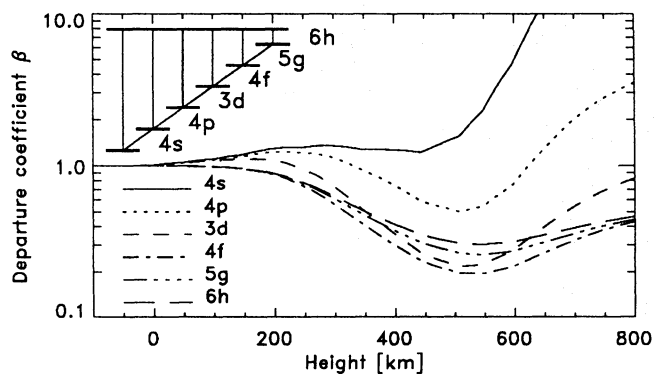
Fig. 10. Departure coefficients for the VAL3-C atmosphere computed with the 6-level-plus-continuum model atom. Inset shows model atom schematically: level separations are not on energy scale, connecting lines mark radiative transitions, all levels photoionize

Fig. 11. Departure coefficients for tailored atoms with increasing number of bound levels plus continuum, and only one line connecting the upper two bound levels. Each model atom shown schematically as inset for each panel. All levels including the continuum are collisionally coupled

Fig. 12. Departure coefficients for the same tailored atoms as indicated in Fig. 11, but now with all lines up to the upper bound level of each atom included. Departure coefficients are only shown for the lowest three levels (4s, top left; 4p, top right; 3d, bottom left), together with the ratio β_{4p}/β_{4s} (bottom right)

overpopulation is surprising since appreciable underpopulation is the rule for minority species which are sensitive to radiative ionization with 3 – 4 eV photons, at least for atmospheres with a cool temperature minimum such as the VAL3-C model. Although the photoionization rate from the 4s ground state is very small due to the small cross-section, there are other violet ionization edges such as the 4p one which should produce overionization by feeding on superthermal radiation fields. In Fe I, for example, the overionization is also produced by levels at intermediate energy in the term diagram, lower levels being less strongly coupled to the continuum because of weaker edge intensities. In Fe I the resulting population loss is redistributed over many levels, producing overall depletion of the neutral ionization stage; this behavior is typical of minority species as evidenced by their population departure graphs in Vernazza et al. (1981). Thus, we need to explain why such an upper-photospheric population depletion does not occur in the alkalis which are minority species in the extreme. The photospheric overpopulations of the alkalis are small (Fig. 6); the discrepancy with other neutral metals lies in their not being underpopulated by a factor of 3 – 5.

Earlier analyses also yielded near-LTE population of K I 4s in the photosphere but without questioning its cause; in fact, LTE opacity was an implicit assumption of the initial NLTE study by De la Reza & Müller (1975). The same pattern is shown by Na I in Fig. 6 with smaller 3s overpopulation; the larger K I 4s and Na I 3s overpopulations in Fig. 7 result from the higher upper-photosphere temperature of the HOLMUL model (J_ν less superthermal in the ultraviolet).

How does the overpopulation come about? The answer lies in a NLTE mechanism which we illustrate with experiments shown in Figs. 10 – 13. Very simplified model atoms are employed in these experiments for clarity. The basic atom is shown as inset in Fig. 10 and contains only six bound K I levels plus the K II ground state as continuum. This model atom, small as it is, furnishes a valid representation of the full K I spectrum in the sense that it contains the major NLTE processes in similar measure. The corresponding departure coefficients shown in Fig. 10 are indeed close to those of the comprehensive model in Fig. 6.

The simple model atom of Fig. 10 was constructed from the transitions with the largest oscillator strengths and photoionization cross-sections in the comprehensive model. This procedure uncovers the presence of a cascade ladder along high-probability infrared lines with quantum number jumps $\Delta L_{ul} = L_u - L_l = 1$.
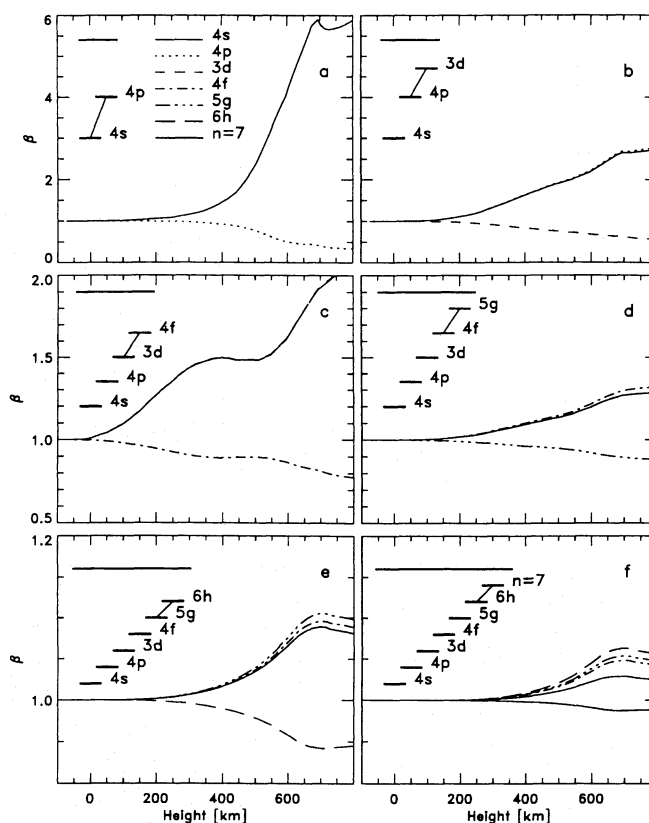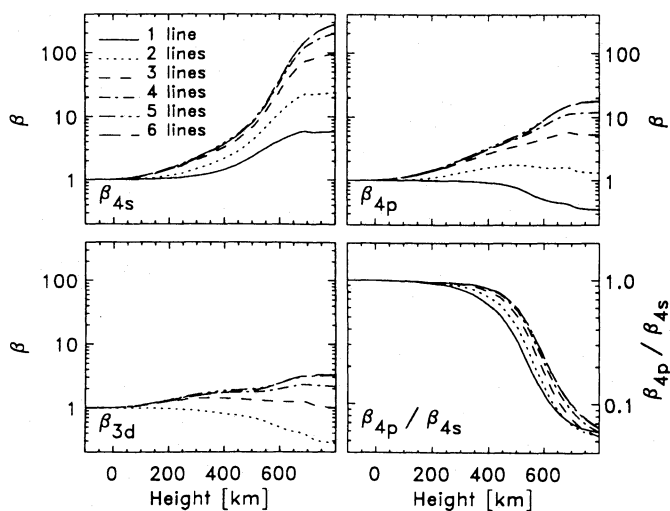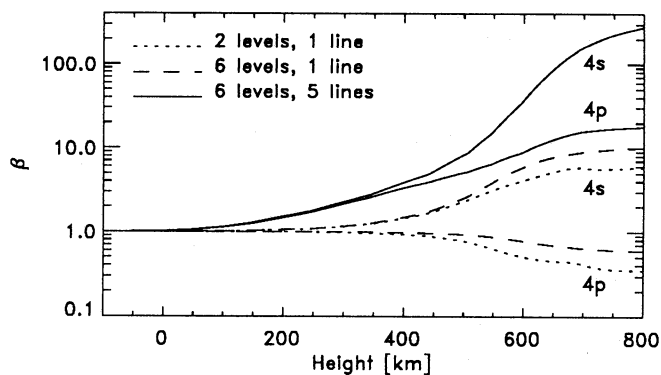
Fig. 13. Departure coefficients for $4s$ and $4p$, for a 2-level plus continuum atom (dotted), a 6-level plus continuum atom with only $4s - 4p$ as radiative transition (dashed), and a 6-level plus continuum atom with all five line transitions (solid)

The K I Grotrian diagram has very regular structure, with strong lines stacked along this ladder; this structure favors constructive adding of photon losses. As we show below, these ladder losses together with the losses in the resonance lines produce overpopulation of the neutral stage in the upper photosphere by causing a downward population-replenisment flow out of the continuum reservoir. We term this process "photon suction" because it is driven by outgoing line photons; their loss produces a $J_\nu < B_\nu$ situation resulting in deficient photoexcitation which is compensated from the reservoir at higher energy. This replenishment flow is balanced by closing the loop to the continuum through net ionization only at sufficient overpopulation of the whole neutral stage. Such suction (or optical siphoning) is just the reverse of fluorescence excitation (optical pumping) in a $J_\nu > B_\nu$ environment: in that case, the atoms gain excitation energy from a superthermal radiation field and so obtain non-thermal overpopulation of high-excitation levels out of a low-excitation reservoir, whereas photon suction results in overpopulation of low-energy levels from a higher-excitation reservoir. In the alkalis, that reservoir is not simply constituted by the upper levels of the resonance lines, as would be the case for a classical two-level atom, but by the next ionization stage; the partitioning between atom and ion is therefore affected, as well as the Rydberg regime along which the replenishment flow occurs. We demonstrate this with a sequence of experiments.

In the textbook problem of a two-level atom with one line (Athay 1972, Ch. 3), resembling K I $4s$ and $4p$ with one resonance line only, resonance scattering ($\epsilon \ll 1$) produces a small source function value at the surface, $S^{\mathrm{L}} \approx \sqrt{\epsilon}\, B_\nu(T_e)$ for a homogeneous atmosphere. The upper level departure coefficient drops deeply below unity while the lower level departure coefficient increases slightly above unity, the magnitude of the departures being inverse to the Boltzmann population ratio.

Adding collisional coupling to a large continuum reservoir, as present for minority species such as K I and Na I, modifies this simple case considerably. The two-level approximation does not apply to minority species at all, because the difference in coupling to the continuum reservoir between the two levels affects the populations strongly even in the absence of radiative imbalances. The collisional ionization rate scales as $\chi_i^{-2} \exp(-5040\,\chi_i/T)$, where χ_i is the ionization energy of level i in electron volts (Allen 1976, p. 42); therefore, the collisional ionization rate is roughly an order of magnitude larger for $4p$ than for $4s$. The

stronger coupling to the continuum forces β_{4p} closer to unity because the reservoir maintains $\beta = 1$ whatever happens to the neutral stage. The resonance line forces β_{4s} to follow this rise so that $4s$ becomes yet more overpopulated. This is demonstrated in Fig. 11a which shows the $4s$ and $4p$ departure coefficients for such a two-level-plus-continuum atom, shown in the inset. The magnitudes of the departures do not scale inversely to the Boltzmann ratio anymore; the $4s$ level, and with it the whole neutral stage, is now strongly overpopulated solely due to the photon losses in the $4s - 4p$ transition. This diagram supplies the basic demonstration of the photon suction phenomenon: strong coupling to the continuum reservoir causes replenishment from that reservoir of any population losses that are imposed by nonlocal conditions (in this case the shortage of impinging line photons), resulting in overpopulation up to the amount at which the net recombination to the upper level is balanced by collisional overionization from the ground state.

The other panels of Fig. 11 apply this two-level description to successively higher lines in the K I Grotrian diagram. The insets show the corresponding model atoms schematically; for each, bound-free coupling to the continuum is only through collisions. Each line similarly imposes overpopulation on the lower levels. The size of the effect in the chromospheric parts of the diagrams decreases steadily with excitation energy, because the disparity between the coupling to the continuum of the upper level and of the lower level decreases (note the ordinate scale changes). In the photosphere there is additional dependence on the height at which the lines start losing photons; near $h = 200$ km the largest change is induced by the $3d - 4p$ transition because the radiation escapes from deep layers at its wavelength ($\lambda = 1.5\ \mu$m, close to the H$^-$ opacity minimum at 1.6 μm). The higher-excitation transitions lie in the far infrared and originate from the upper photosphere, with the free-free H$^-$ continuum. We have also extended these experiments beyond the levels and lines of the comprehensive model, finding that the impact of photon losses in yet higher lines on the lower-level populations is negligibly small.

Figure 12 shows results from a similar experiment in which the level-adding procedure was followed for the same sequence, but now increasing the number of lines with each extra level as well, again from the bottom up. The figure combines results from the different model atoms into graphs of departure coefficients, for clarity limited to the levels $4s$, $4p$ and $3d$. Their departure coefficients show a clean upward progression with increasing line number, the divergence between the curves becoming smaller and smaller. Thus, the lower-line photon losses have the largest effect. The plots also show that adding levels above $6h$ is not necessary to correctly describe photon suction since the topmost increment is already negligible. The lower right panel shows that the β_{4p}/β_{4s} ratio increases with the number of lines: the curves shift to the right because the drop of β_{4p} due to resonance-line photon losses occurs higher in the atmosphere for larger resonance-line opacity.

A final experiment is shown in Fig. 13, comparing the resonance-line suction to the suction given by the full ladder of high-gf lines. This experiment shows that the photon losses in the resonance line alone are insufficient to produce the overpopulation of the comprehensive atom, even if collisional cascading along levels $6h$, $5g$, $4f$ and $3d$ provides an extra channel to populate $4p$ from the K II ground state. Thus, the photon losses in the high-gf infrared lines in the ladder contribute significantly to driving the total net recombination flow from the continuum.
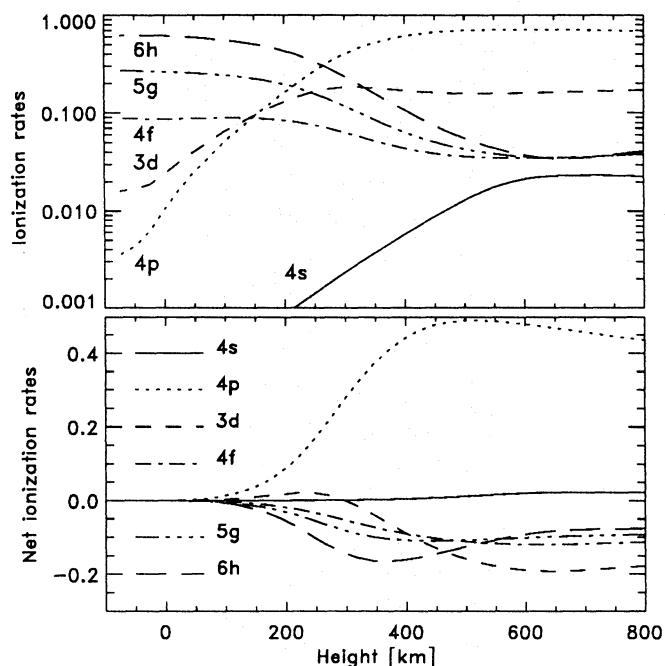
Fig. 14. Ionization rates (top) and net rates (bottom) for the indicated levels, normalized with the total ionization rate
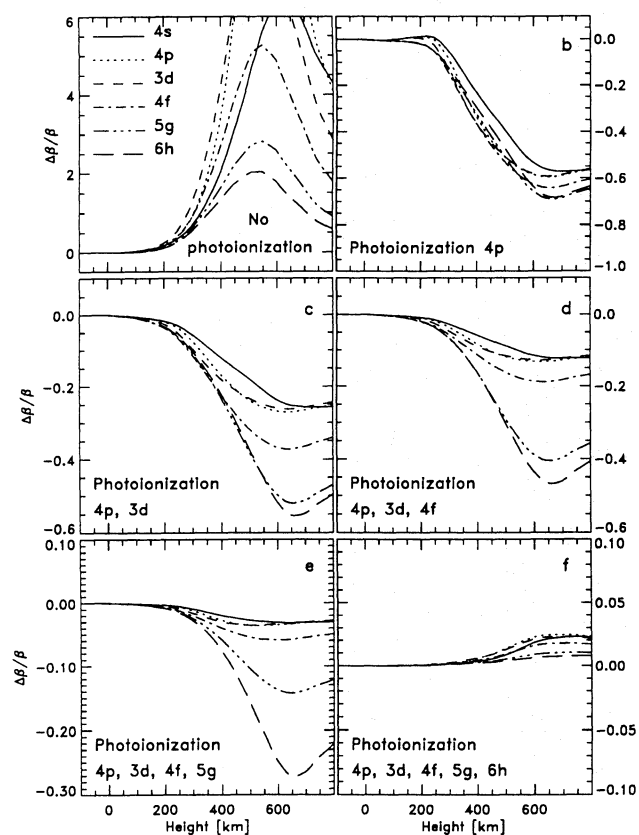

Fig. 15. Photoionization progression, showing departure coefficient changes relative to results in Fig. 10 for increasing participation in photoionization. Ionization is progressively added level-by-level from $4p$ up, as specified. Note vertical scale changes. The small remaining differences in panel f are due to not-included photoionization from the $4s$ ground state
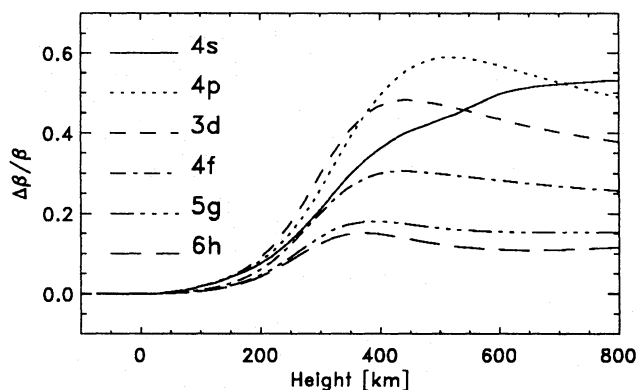

Fig. 16. Departure coefficients for 6 level atom with hydrogenic frequency-dependence of α_ν^{4p} relative to results for same atom with detailed frequency-dependence as in comprehensive model

4.2.3. Ultraviolet overionization

We next discuss ultraviolet overionization, which establishes statistical equilibrium by counteracting the suction flow. As discussed above, bound-free photoionization from the $4s$ ground level should normally cause marked overionization because its edge lies near 300 nm where J_ν is larger than $B_\nu(T_e)$ in the VAL3-C continuum, but it is actually negligibly small due to the quantum-mechanical cancellations that reduce its threshold cross-section. Consequently, the ionization takes mainly place from the $4p$ levels.

The same simple 6-level-plus-continuum model atom shown in the inset of Fig. 10 serves to investigate the radiative ionization and recombination processes in K I. Figure 14 shows normalized upward ionization rates per level (upper panel) and net rates per level (lower panel), in both cases combining radiative and collision rates. The figure indicates that $4p$ and $3d$ largely determine the ionization equilibrium in the upper atmosphere where they have the largest contribution and also the largest imbalances; in the deeper photosphere, ionization is dominated by collisional transitions from high-excitation levels such as $5g$ and $6h$ (upper panel), with detailed balancing (lower panel). The break between these regimes lies near $h = 250$ km; its location is not very sensitive to the collision cross-sections because the collision rates are proportional to the electron density, which steeply decreases with height.

An ionization experiment is shown in Fig. 15, displaying the changes of departure coefficients (relative to those in Fig. 10, where all photoionization transitions are included) which result from successively adding photoionization transitions. Without any photoionization (panel a), the photon suction along the line ladder results in very large overpopulations, statistical equilibrium only being reached when the populations are sufficiently large to close the loop by net collisional ionization. Adding photoionization from $4p$ drastically alters the result (panel b, note scale change). Since this transition feeds on superthermal radiation, a much smaller K I population suffices to balance the suction flow; in fact, the relative change reverses sign. The remaining panels show the effects of the higher levels which have net recombination (Fig. 14). Adding these brings down more electrons from the continuum which cascade down in the large-probability lines and require a larger $4p$ population to to produce statistical equilibrium with the ion then when these recombination flows

are neglected. They are small in comparison, however; the largest effect occurs when the $3d$ photoionization is included. Thus, the major NLTE rate from the continuum down is the suction flow driven by photon losses; the balancing flow is governed by net photoionization from $4p$ which is sensitive to the $J_\nu - B_\nu(T_e)$ radiation imbalance at $\lambda \approx 450$ nm.

4.2.4. Overrecombination

Overrecombination may be expected for photoionization transitions from levels close to the continuum, because in the deep photosphere the angle-averaged intensity J_ν drops below the Planck function at infrared wavelengths if the temperature gradient is not too steep (cf. Fig. 3). Such transitions would have a deficiency in ionizing photons and produce net recombination. The process may produce high-level overpopulations; in our computations, however, overpopulations do not occur because the suction flow dominates. The latter also causes net recombination but maintains underpopulation along the ladder down to $4p$. The $3d$ level produces net recombination primarily because it is underpopulated, not because of a radiation imbalance ($J_\nu \approx B_\nu$).

The overall partitioning between K II and K I depends on the atmospheric model primarily via the $4p$ photoionization. The suction flow is line-driven and occurs about similarly in different models since the outward density decay is so steep that the line opacity scaling is not very sensitive to model changes. The $4p$ photoionization, however, uses ultraviolet radiation near $\lambda = 450$ nm that is superthermal and overionizing in cool-minimum models as the VAL3-C, but which is about thermal in models with a less steep temperature gradient in the upper photosphere such as the HOLMUL model. For the latter, $4p$ requires a larger overpopulation to balance the suction flow; this explains the larger departure coefficients around $h = 500$ km in Fig. 7 compared with Fig. 6. Likewise, the partitioning depends sensitively on the $4p$ photoionization cross-section α_ν^{4p}, and also on the ratio $\alpha_\nu^{4p}/\alpha_\nu^{3d}$ since the corresponding net rates compete.

A final ionization experiment concerns the frequency dependence of the photoionization cross-sections. Figure 16 shows for the 6-level-plus-continuum atom that replacing the adopted α_ν^{4p} frequency dependence by hydrogenic ν^{-3} decay produces an increase of about 40% of the ground state population. This increase affects the opacity of the resonance lines by the same amount, but the change for $4p$ is similar so that the resonance line source functions are only slightly affected.
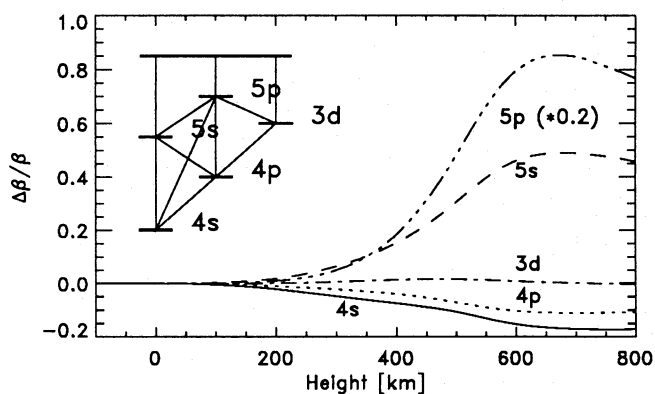

Fig. 17. Departure coefficients for 6 level atom indicated in inset relative to results for same atom without $4s - 5p$ transition
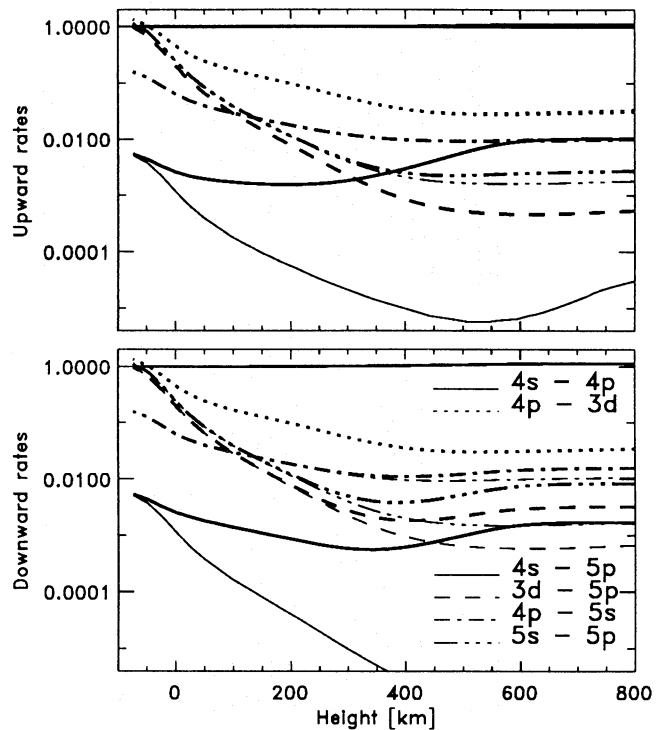

Fig. 18. Rates for 6 level atom indicated in inset of fig. 17; upper panel: normalized total upward rates ($n_l P_{lu} = n_l(R_{lu} + C_{lu})$); lower panel: normalized downward rates rates ($n_u P_{ul}$). Thick lines are for the case with $4s - 5p$ pumping transition, thin lines for the case without. The normalization is for both panels given by the upward rate in the resonance line when the $4s - 5p$ line is present. Coding: $4s - 4p$ and $4s - 5p$ solid, $4p - 3d$ dotted, $3d - 5p$ dashed, $4p - 5s$ dot-dashed, $5s - 5p$ dotted-dashed

4.2.5. Optical line pumping

Optical line pumping is the bound-bound analogon of ultraviolet overionization, superthermal radiation of non-local origin producing enhanced excitation. In the K I spectrum there is only one violet line of interest, namely the $4s - 5p$ transition at 404.5 nm. It is pumped by $J_\nu - B_\nu(T_e)$ excess radiation from below. Again, this pump operates in photospheres with a steep temperature decrease since that sets the $J_\nu - B_\nu(T_e)$ excess. The $5p$ level departure curves (Figs. 6 and 7) show an early outward rise due to this enhanced excitation; it is more pronounced for VAL3-C than for the HOLMUL model. The presence of a chromosphere is irrelevant to this line because it becomes optically thin in the photosphere.

To demonstrate the pumping in more detail we employ the simplest realistic atom that includes this line. It is shown as inset in Fig. 17 and contains five bound levels plus continuum; the same atom was used by Gomez et al. (1987a, 1991). Fig. 17 shows departure coefficients for this atom relative to the departures obtained from the same atom without the $4s - 5p$ pump. The effect of the pumping is largely limited to the $5p$ population; note that its departure change has been scaled down to fit the figure. The changes are smaller for the lower levels because a given Δn produces a smaller relative change $|\Delta n/n|$ for levels with larger population n. Figure 18 shows relevant rates, for the case with pump (thick lines) and the case without pump (thin). The pump barely changes the upward rates except for the pumping transition itself, but it does influence the downward

rates, especially for the downward transitions from $5p$. Therefore, the $5p - 3d$ and $5p - 5s$ transitions, which have high transition probability, carry away part of the extra rate populating $5p$ to enhance the populations of $3d$ and $5s$. The $5s$ population is enhanced more than the $3d$ population because the $5p - 5s$ transition has higher probability than $5p - 3d$, while $5s - 4p$ has smaller probability than $3d - 4p$. In addition, $4p$ and $3d$ are coupled more strongly to the continuum reservoir than $5s$ so that they change less. The resonance lines force $\beta_{4p} \approx \beta_{4s}$. Thus, the net result is a small decrease of the lower-level β's and larger increase of β_{5p} (Fig. 17).
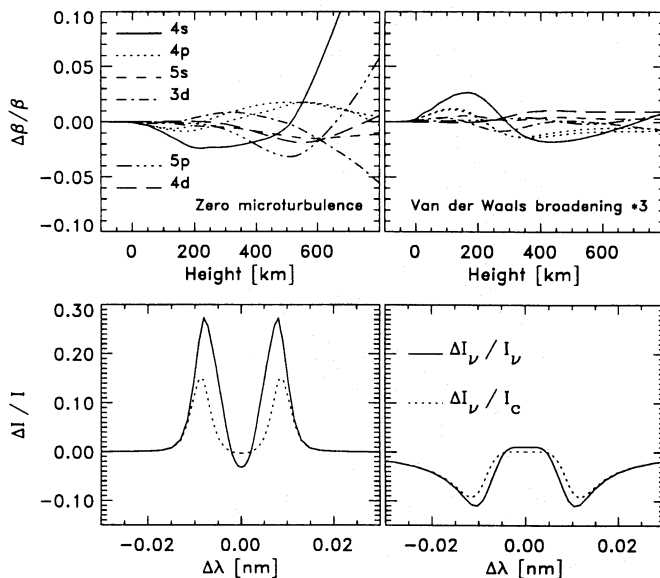
Fig. 19. Departure coefficients for 6 lowest levels (top row) and resonance line profiles (bottom row) for zero microturbulence (left) and enhanced Van der Waals broadening (right), relative to comprehensive results with VAL3-C microturbulence and standard Van der Waals broadening

4.3. NLTE in K I

After the above identification of the various NLTE processes that participate in the formation of the K I 769.9 nm line, we can now interpret all features present in Figs. 6 and 7.

The rise of the departure coefficients which sets in near $h = 100$ km is due to the joint effect of line photon losses in the resonance lines and in the high-probability infrared lines higher up in the Grotrian diagram. The effect is largest for the lowest levels, $4s$ and $4p$, which profit most from this photon suction process. The resonance line photon losses start slightly higher in the atmosphere than the losses in the infrared lines; as a result, β_{4s} and β_{4p} rise together initially while β_{4p} starts dropping off at $h \approx 200$ km. This shift is small although the resonance lines have much larger opacity than the infrared lines because the former scatter strongly, maintaining a photon drain from far below their optical depth unity location.

The photon suction competes with photoionization and recombination in setting the departure coefficients over most of the atmosphere. Level $4p$ is the prime ionizing level. The ionization rate out of this level senses any imbalance between J_ν and $B_\nu(T_e)$ in the near ultraviolet. The VAL3-C model has J_ν larger than $B_\nu(T_e)$ in the temperature minimum region; this imbalance results in the depression of β_{4p} in Fig. 6 which is shared by all

other β's. Above $h \approx 600$ km, J_ν is smaller than $B_\nu(T_e)$ so that all β's increase again into the chromosphere. Due to the photon suction they would also increase without contribution from the $J_\nu - B_\nu(T_e)$ imbalance, as demonstrated by the outward increasing overpopulation in Fig. 12, but the chromospheric ionization balance has larger influence. This is evident from the results for the HOLMUL model in Fig. 7, in which the absence of a chromosphere causes J_ν to be considerably larger than $B_\nu(T_e)$ in the upper parts of the atmosphere. This reversed radiation imbalance produces overionization and appreciable depression of the departure coefficients above $h \approx 600$ km.

The departure coefficient of $3d\ ^2D^e$ exhibits a deep minimum in Fig. 6 because it sustains the net flow to $4p$ which balances the overionization out of that level. The major part of that flow comes along the suction ladder (Fig. 11); a smaller part recombines directly from the continuum (Fig. 14) because the net recombination scales as $\int_{\nu_0}^{\infty}(B_\nu - (\beta_{3d}/\beta_c)J_\nu)\,d\nu$ and the bound-free edge is at 742.1 nm where $J_\nu \approx B_\nu$ in the photosphere. The $3d$ deficit does not impede further cascade to $4p$ because the $3d - 4p$ transition has high oscillator strength and yet is optically thin. In contrast, the bound-free edge of $4p$ at 455 nm is characterized by an appreciable $J_\nu - B_\nu(T_e)$ excess; this excess is large enough to provide net ionization from a yet underpopulated $4p$ level. The same behavior is present in the upper layers of the HOLMUL model (Fig. 7) because these have similar radiation field imbalances as the temperature minimum region of the VAL3-C model.

The precise behavior of the other K I departure coefficients is a result of the interplay of radiative ionization and recombination, line photon losses and optical pumping. Level $5p$ feels a rather cool ionizing radiation field and is sensitive to the optical pumping from $4s$; in the photosphere, β_{5p} therefore couples closely to β_{4s}. De-excitation from $5p$ goes through $5s$ and $3d$, increasing those populations above their pump-less values. In addition, $3d$ is strongly coupled to $4p$ by a strong line with large photon losses; the divergence of β_{3d} from β_{4p} is set by the latter. The large drop of β_{3d} promotes large net recombination flow into $3d$. The higher levels are coupled closer to the population reservoir in the K II ground state and experience the infrared $J_\nu < B_\nu(T_e)$ imbalance already in the photosphere; their photon loss drain is smaller than for $3d$ and the precise values of these higher-level departures are sensitive to the corresponding photoionization cross-sections.

The K I resonance line source function shown in the middle-left panels of Figs. 6 and 7 behaves virtually independently from all other processes; the line opacity is determined primarily by the balance between net photoionization on one hand (mainly from $4p$) and the amount of net recombination into other levels and of suction flow along the ladder on the other hand. This balance is sensitive to atomic parameters, as shown in Fig. 16 by changing the $4p$ photoionization cross-section. The ground level overpopulation that results from these processes moves the formation of the resonance lines upward in the atmosphere, but not enough to shift it to the chromosphere; the line does not show the chromospheric source function rise in its profile, not even for LTE. The main difference between LTE and NLTE formation is the depression of the line core intensity due to the lower NLTE source function.

A final K I formation issue concerns line broadening and its influence on the populations. Of particular interest are the sensitivities of the source function and the opacity of the resonance lines to microturbulence and Van der Waals broadening.

We remind the reader that, sofar, we employed the microturbulence specified with each atmospheric model and no damping enhancement factor at all. Figure 19 displays VAL3-C departure coefficient changes (top) and line profile changes (bottom) for zero microturbulence (left) and damping enhancement factor 3 (right), respectively. Each panel shows results relative to the comprehensive-model results in Fig. 6. The damping enhancement is the same as the one advised by Holweger & Müller (1974) and used by Gomez et al. (1991). Obviously, the line profile changes considerably in both cases since both parameters enter directly into the line extinction profile. Indirectly, they also modify the location of the line-center $\tau_{v_0} = 1$ location. The changes in the departure coefficients and the line source function (related through Eq. 4) are much smaller, implying that the statistical equilibrium is relatively insensitive to changes in these parameters.

4.4. NLTE in Na I

The sodium Grotrian diagram is very similar to the potassium Grotrian diagram (cf. Figs. 4 and 5). Most of the discussions above therefore also hold for Na I and its resonance lines. The differences mainly result from the different atomic parameters: the larger Na I abundance (6.31 instead of 5.13), the larger Na I photoionization cross-sections for the lower levels, the smaller Na I oscillator strengths, the larger Na I ionization energy, and the wavelength differences between corresponding spectral lines and continuum edges. There is a close relation between the oscillator strengths; the Na I oscillator strengths for equivalent transitions, e.g. comparing Na I and K I $4s - 4p$, are typically larger by a few tens of percents for stronger lines and by up to an order of magnitude for the weaker lines. However, the Na I oscillator strengths are slightly smaller, with a few exceptions, when one compares oscillator strengths at equivalent locations in the Grotrian diagram with respect to the resonance lines. One of the exceptions is the Na I $3s - 4p$ line. This ultraviolet pumping line has a gf-value 1.5 times larger than the K I $4s - 5p$ pump. Furthermore, the Na I $3s - 3d$ line is two orders of magnitude stronger than its K I counterpart, and also sensitive to optical pumping.

The Na I photon suction effect occurs higher in the atmosphere than for K I due to the larger sodium abundance; the split between β_{3s} and β_{3p} starts only just below the temperature minimum, where photoionization plays an important role as well. In the photosphere there is less overionization in Na I than in K I, as evidenced by the departure coefficients for the upper levels of the resonance lines in the top panels of Fig. 6. This may seem in conflict with the larger photoionization cross-section of the lower levels in Na I; indeed, for model atoms containing only the lowest levels Na I has more overionization than K I. However, with increasing number of levels this overionization is strongly reduced due to stronger photon suction in Na I.

As in K I, the departure coefficient of Na I $3d$ drops to very small values, i.e. large underpopulation, for the same reason. It drops even deeper than in K I because the coupling of $3d$ to the upper level of the resonance lines is weaker and because it is fed less from Na I $4p$ than the K I $3d$ level is fed from K I $5p$. Due to the larger Na I ionization energy, all characteristics of the K I ionization and recombination shift upward in the Na I Grotrian diagram; therefore, the Na I β_{4f} coefficient drops deep as well. The deep drops cause considerable net radiative recombination into the Na I $3d$ and $4f$ levels.
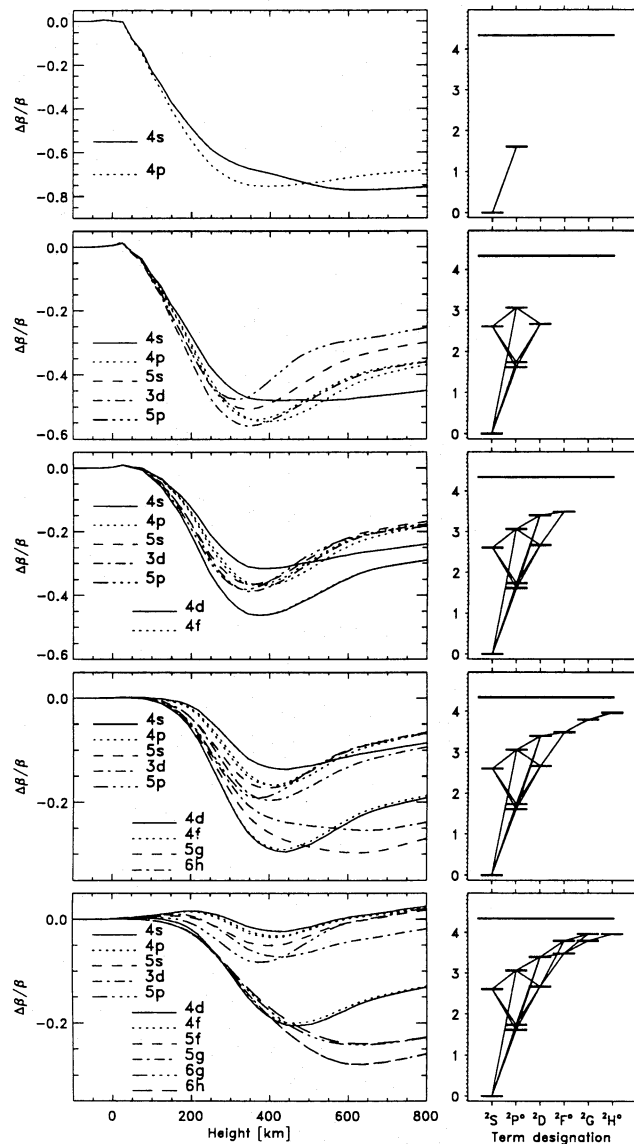

Fig. 20. Departure coefficients for simplified 5 K I atoms: respectively 2, 6, 8, 10 and 12 bound levels plus continuum. All are relative to the comprehensive model. Note the scale changes

The Na I ultraviolet pumping line $3s - 4p$ is stronger than its K I equivalent, but its impact on the departure coefficients is much smaller; the hot ultraviolet radiation field in the line wings adds only a small fraction to the total excitation rate. However, in Na I there are other lines influenced by optical pumping, especially the transitions from the $3s$ and $3p$ levels to the highest levels in the term diagram. The lines from $3s$ and $3p$ to $n = 7$ are the most important. Together, these produce a $5 - 10\%$ reduction of the lower level departure coefficients, which directly enters the line opacities.

The NLTE Na I D line source functions drop below the local Planck function well below line optical depth unity, but not as deep in the atmosphere as for K I 769.9 nm due to the larger sodium abundance. The Na I D lines scatter more strongly than the K I resonance lines, which is evident in the smaller fraction S^L/B_{v_0} at large height. Their NLTE line source functions decrease
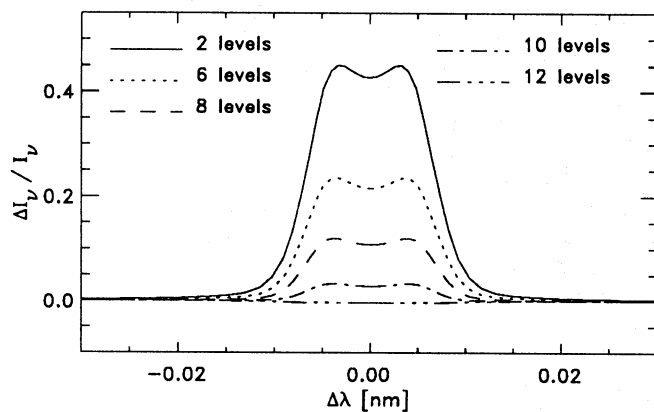
Fig. 21. Resonance line profiles for 5 K I atoms: respectively 2, 6, 8, 10 and 12 bound levels plus continuum. All are relative to the comprehensive model

monotonically outward, producing line profiles without emission cores.

4.5. Confection atoms

We are now in a position to define "confection atoms", i.e. appropriately simplified model atoms that are easier to handle than our comprehensive model atoms, but yet contain the essential population mechanisms. Such confection models are useful in large-volume modeling, for example in multi-dimensional and/or time-dependent numerical simulations. We discuss suitable choices in this section, first for K I, then for Na I.

The basic behavior of the K I resonance line is described by only two bound levels that govern its resonance scattering. The processes of radiative overionization, radiative overrecombination and the photon-loss driven suction flow modify this simple picture, warranting the addition of several more levels and lines. The presence of ns levels is not required except for $5s$, which is at the receiving end of the most probable de-excitation channel from the $5p$ level. The ionization balance is set mainly by levels $4p$ and $3d$ which are therefore indispensable, and further by the collective effect of the high-gf infrared lines higher up in the Grotrian diagram which were shown to be an important ingredient in Sect. 4.2. Actually, there are two such ladders of infrared lines which lead down into important lower levels. The other chain, not modeled above, consists of the K I levels $5p$, $4d$, $5f$ and $6g$.

How many levels and lines should be included? Figure 20 shows VAL3-C changes of departure coefficients, again all relative to the results for the comprehensive model shown in Fig 6, for atoms with increasing numbers of levels, from the basic 2-level-plus-continuum atom with only one line to a rather sophisticated 12-level-plus-continuum atom with 20 lines.

The simpler atoms have already nearly correct resonance line source functions, evident in similar changes for $4s$ and $4p$, but considerably less recombination in the upper photosphere so that the resonance lines are formed too deep. The changes of the corresponding resonance line profiles relative to the results for the comprehensive model (bottom of Fig. 6) are shown in Fig. 21. The two-level atom indeed produces too shallow profiles; the intensity changes are smaller than the population changes because the line formation region shifts by no more than a scale height and the line source function does not vary strongly over that interval.
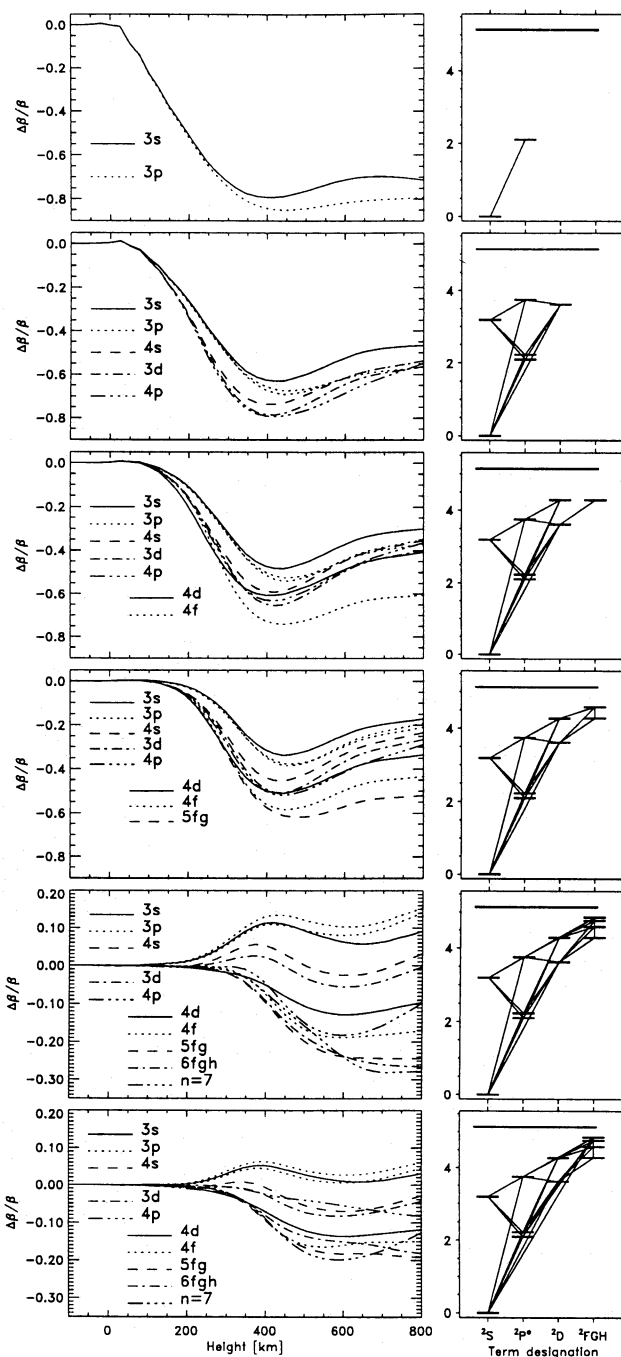

Fig. 22. Departure coefficients for simplified 6 Na I atoms: respectively 2, 6, 8, 9, and two atoms with 11 bound levels plus continuum. All are relative to the comprehensive model. Note the scale changes

The larger atoms progressively approach the results from the comprehensive atom; Figs. 20 and 21 portray a gallery from which model atoms may be selected trading precision against size.

For Na I we provide a similar range of models in Figs. 22 and 23, again from a simple 2-level-plus-continuum one-line atom to an 11-level-plus-continuum atom with 29 lines. The build-up again reflects the preferred excitation and de-excitation channels along lines $\Delta L = 1$. The results are again shown as VAL3-C
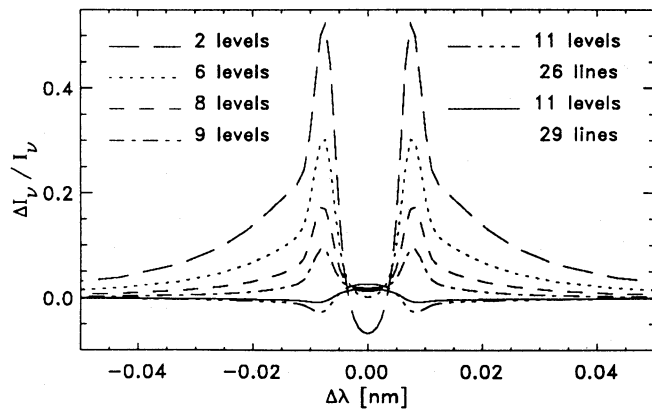
Fig. 23. Na I D_1 resonance line profiles for 6 Na I atoms: respectively 2, 6, 8, 9 and two atoms with 11 bound levels plus continuum. All are relative to the comprehensive model

departure coefficient changes (Fig. 22) and Na I D_1 line profile changes (Fig. 23), relative to the comprehensive results in Fig. 6. The whole range produces fairly good resonance line source functions (equality of β_{3p} and β_{3s} curves), but only poor to moderate line opacities (deviation of β_{3s} from unity). The latter discrepancies again produce sizable line profile disagreements. Only the largest model produces acceptable results.

Note that in the fifth row of Fig. 22 the pumping transitions between the lowest five levels and the $n = 7$ level are omitted, resulting in considerable overpopulation of the lower levels with respect to the comprehensive model. The bottom panels additionally include the two pumping transitons from $3s$ and $3p$ to the $n = 7$ level; these are the only ones needed to represent the pumping in Na I properly.

Finally, these figures show also to what extent the smaller model atoms employed in earlier NLTE analyses of alkali line formation depart from complete descriptions. The K I analyses of Gomez et al. (1987a, 1991) used the model atom in the second row of Fig. 20; their departure coefficients are indeed close to ours if we apply the relevant corrections to our comprehensive-atom results. The corrections are larger for the opacity of the 769.9 nm resonance line (about 50%) than for the line source function (10%) and result in line-center intensities that are about 20% too high. Gomez et al. (1991) performed differential sensitivity experiments which are less susceptible to these errors than line profile fits; however, the smaller atom also lacks part of the temperature sensitivity of the photoionization and photon suction processes.

Gehren (1975) used a Na I model atom that resembles the one in the third row of Fig. 22, also including levels $5s$ and $5p$ which do not affect the NLTE behavior of the lower levels. The $5p$ photoionization edge in the near infrared gives small over-recombination, but the absence of an efficient downward channel restricts its influence to the upper part of the term diagram. Again there are differences of about 50% in the opacity of the resonance lines and of 10% in their source functions. Gehren noted that his atom was too small to contain the recombination flow which cascades down through the higher levels. The model employed by Caccin et al. (1980) was somewhat simpler than Gehren's and neglects the photon suction flow entirely. It includes level $5s$ but misses $4f$ which is more important. The results are intermediate between those in the second and third row of Fig. 22.

5. Conclusion

The formation of the alkali spectra turns out to be complex. In very first approximation the resonance lines are well described by two-level resonance scattering alone, but their opacities are sensitive to a complicated NLTE ionization balance in which various NLTE mechanisms compete, and in addition to optical pumping of line transitions. These mechanisms are probably ubiquitous; for example, the photon suction mechanism described here operates also in the solar Mg I spectum where it contributes to the formation of the infrared Mg I emission features near 12 μm (Carlsson et al. 1992). It should work in the upper term diagram of any neutral minority species of which the continuum represents a LTE reservoir from which high-lying levels can replenish population depletion processes at lower excitation energy. In the alkalis, the whole Grotrian diagram is within reach of the continuum influence; in neutral metals of higher ionization energy such as Mg I, only the upper part.

A difference between the alkalis and the more abundant neutral metals is that the alkali lines become effectively thin already in the photosphere, where the strongest Fe I and Mg I resonance lines, for example, are still in detailed balance. This is the reason that the complex ionization balance affects the alkali resonance lines, while Fe I has much simpler overionization and suction is evident in Mg I only in infrared high-excitation lines. The basic properties of the alkalis are therefore that all their levels except the ground state are relatively strongly coupled to the LTE continuum reservoir on the one hand, but that the strongest lines become optically or at least effectively thin already in the photosphere, with the attendent effects of NLTE photon losses.

Finally, our K I analysis above has procedural interest for line formation studies in general. We have found once again that it is difficult to interprete results from a multi-level statistical-equilibrium solution for situations in which different population and depopulation mechanisms and channels compete. This conclusion agrees with the studies of Skumanich and Lites (1985, 1986) who suggest two-level interpretation of multi-level results and apply this to the solar hydrogen spectrum, in particular the complex formation of Hα. We have not implemented their scheme; our solution has been to build up skeleton atomic models from a two-level configuration upward, while simultaneously stripping down a large comprehensive model. The latter technique is the one used traditionally to find out which transitions are less important for the overall solution, but it often fails to demonstrate what the essential mechanisms are because different atomic models may yield similar equilibrium configurations in different manner. We have found it helpful to employ the build-up approach in determining the physical nature of the NLTE population mechanisms. Our examples in Sect. 4.2 illustrate its use and suggest that such simultaneous skeleton-model build-up and comprehensive-model strip-down represents a valuable approach for other NLTE radiation transfer problems as well.

References

Allen, C. W. 1976, Astrophysical Quantities, Athlone Press, University of London

Anders, E., Grevesse, N. 1989, Geochim. Cosmochim. Acta, 53, 197

Andersen, B. N., Barth, S., Hansteen, V., Leifsen, T., Lilje, P. B., Vikanes, F. 1985, Solar Phys., 99, 17

Athay, R. G. 1972, Radiation Transport in Spectral Lines, Reidel Publ. Co., Dordrecht

Athay, R. G., Canfield, R. C. 1969, ApJ, 156, 695

Athay, R. G., Lites, B. W. 1972, ApJ, 176, 809

Auer, L. H., Heasley, J. N., Milkey, R. W. 1972, A Computational Method for the Solution of Non-LTE Transfer Problems by the Complete Linearization Method, Contribution No. 555, Kitt Peak National Observatory

Aymar, M. 1978, J. Phys. B, 11, 1413

Aymar, M., Luc-Koenig, E., Combet Farnoux, F. 1976, J. Phys. B: Atom. Molec. Phys., 9, 1279

Bates, D. R., Damgaard, A. 1949, Phil. Trans. R. Soc. London, 242, 101

Beckers, J. M., Mauter, H. A., Mann, G. R., Brown, D. R. 1972, Solar Phys., 25, 81

Bely, O., van Regemorter, H. 1970, ARA&A, 8, 329

Biémont, E., Grevesse, N. 1973, Atomic Data and Nuclear Data Tables, 12, 217

Blamont, J.-E. 1953, Comptes Rendus Acad. Sci., 237, 1320

Blamont, J.-E., Chanin, M.-L. 1968, Compt. Rendus Acad. Sc. Paris, 266, B514

Blamont, J. E., Roddier, F. 1961, Phys. Rev. Lett., 7, 437

Bonet, J. A., Marquez, I., Vazquez, M. 1989, in R. J. Rutten, G. Severino (eds.), Solar and Stellar Granulation, NATO ASI Series C-263, Kluwer, Dordrecht, p. 299

Bonet, J. A., Marquez, I., Vazquez, M., Wöhl, H. 1988, A&A, 198, 322

Brookes, J. R., Isaak, G. R., van der Raay, H. B. 1976, Nature, 259, 92

Brookes, J. R., Isaak, G. R., van der Raay, H. B. 1978, MNRAS, 185, 1

Burgess, A., Seaton, M. J. 1960, MNRAS, 120, 121

Butler, K., Mendoza, C. 1983, J. Phys. B, 16, L707

Cacciani, A., Fofi, M. 1978, Solar Phys., 59, 179

Cacciani, A., Smith, E., Zirin, H. 1991, in L. J. November (ed.), Solar Polarimetry, Proc. 11th NSO/SP Summer Workshop, National Solar Observatory, Sunspot, p. 133

Cacciani, A., Varsik, J., Zirin, H. 1990, Solar Phys., 125, 173

Caccin, B., Gomez, M. T., Roberti, G. 1980, A&A, 92, 63

Carlsson, M. 1986, A Computer Program for Solving Multi-Level Non-LTE Radiative Transfer Problems in Moving or Static Atmospheres, Report No. 33, Uppsala Astronomical Observatory

Carlsson, M., Rutten, R. J., Shchukina, N. G. 1992, A&A, 253, 567

Chamaraux, P. 1967, Ann. d'Astrophys., 30, 67

Chang, J. J., Kelly, H. P. 1972, Phys. Rev. A, 5, 1713

Cimino, M., Cacciani, A., Sopranzi, N. 1968, Solar Phys., 3, 618

Claverie, A., Isaak, G. R., McLeod, C. P., van der Raay, H. B., Roca-Cortés, T. 1982, Solar Phys., 74, 51

Corliss, C., Sugar, J. 1979, J. Phys. Chem. Ref. Data, 8, 1109

Cram, L. E. 1978, A&A, 70, 345

Cram, L. E., Brown, D. R., Beckers, J. M. 1977, A&A, 57, 211

Curtis, G. W., Jefferies, J. T. 1967, ApJ, 150, 1061

Deubner, F.-L. 1974, in R. G. Athay (ed.), Chromospheric Fine Structure, IAU Symposium 56, Reidel, Dordrecht, p. 263

Deubner, F.-L., Fleck, B. 1989, A&A, 213, 423

Ditchburn, R. W., Jutsum, P. J., Marr, G. V. 1953, Proc. Roy. Soc. London, A 219, 89

Drawin, H. W., Emard, F. 1977, Physica, 85c, 333

Elsworth, Y., Howe, R., Isaak, G. R., McLeod, C. P., New, R. 1990, Nat, 345, 322

Evans, J. C., Testerman, L. 1975, Solar Phys., 45, 41

Fano, U., Cooper, J. W. 1968, Rev. Mod. Phys., 40, 441

Fossat, E., Roddier, F. 1971, Solar Phys., 18, 204

Gabriel, A. H., Bocchia, R., Bonnet, R. M., Cesarsky, C., Christensen-Dalsgaard, J., Damé, L., Delache, P., Deubner, F.-L., Foing, B., Fossat, E., Fröhlich, C., Gorisse, M., Gough, D., Grec, G., Hoyng, P., Pallé, P., Paul, J., Robillot, J.-P., Roca Cortes, T., Stenflo, J. O., Ulrich, R. K., van der Raay, H. B. 1989, in The SOHO Mission – Scientific and Technical Aspects of the Instruments, ESA SP-1104, Paris, p. 13

Gaupp, A., Kuske, P., Andrä, H. J. 1982, Phys. Rev. A, 26, 3351

Gehren, T. 1975, A&A, 28, 289

Gomez, M. T., Marmolino, C., Roberti, G., Severino, G. 1987a, A&A, 188, 169

Gomez, M. T., Marmolino, C., Roberti, G., Severino, G. 1987b, Solar Phys., 112, 227

Gomez, M. T., Rutten, R. J., Severino, G. 1991, A&A, 244, 501

Grec, G., Fossat, E., Pomerantz, M. A. 1983, Solar Phys., 82, 55

Grec, G., Fossat, E., Vernin, J. 1976, A&A, 50, 221

Gulyaev, R. A. 1978, SvA, 22, 719

Gulyaev, R. A. 1983, Astrometriya Astrofiz., 48, 25

Gurtovenko, E. A., Kondrashova, N. N. 1980, Solar Phys., 68, 17

Hofsaess, D. 1979, Atomic Data and Nuclear Data Tables, 24, 285

Holweger, H. 1967, Zeitschr. f. Astrophysik, 65, 365

Holweger, H. 1971, A&A, 10, 128

Holweger, H., Müller, E. A. 1974, Solar Phys., 39, 19

Hudson, R. D., Carter, V. L. 1965, Phys. Rev. A, 139, 1426

Hudson, R. D., Carter, V. L. 1967a, J. Opt. Soc. Am., 57, 651

Hudson, R. D., Carter, V. L. 1967b, J. Opt. Soc. Am., 57, 1471

Isaak, G. R., McLeod, C. P., Pallé, P. L., van der Raay, H. B., Roca-Cortés, T. 1989, A&A, 208, 297

Jefferies, J. T. 1968, Spectral Line Formation, Blaisdell, Waltham, Mass.

Jefferies, S. M., Pallé, P. L., van der Raay, H. B., Regulo, C., Roca-Cortés, T. 1988, Nature, 333, 646

Johnson, H. R. 1962, Ann. d'Astrophys., 25, 35

Kunc, J., Zgorzelski, M. 1977, Atomic Data and Nuclear Data Tables, 19, 1

Kurucz, R. L. 1974, ApJ, 188, L21

Laughlin, C. 1978, J. Phys. B, 11, 1399

Lindgård, A., Nielsen, S. E. 1977, Atomic Data and Nuclear Data Tables, 19, 533

Lites, B. W. 1972, Observation and Analysis of the Solar Neutral Iron Spectrum, NCAR Cooperative Thesis No. 28, High Altitude Observatory, Boulder

LoPresto, J. C., Pierce, A. K. 1985, Solar Phys., 102, 21

Lotz, W. 1966, ApJS, 14, 207

Lotz, W. 1967, Zs. f. Physik, 206, 205

Lotz, W. 1968, Zs. f. Physik, 216, 241

Maltby, P., Avrett, E. H., Carlsson, M., Kjeldseth-Moe, O., Kurucz, R. L., Loeser, R. 1986, ApJ, 306, 284

Marmolino, C., Roberti, G., Severino, G. 1987, Solar Phys., 108, 21

256

Marmolino, C., Roberti, G., Severino, G. 1988, in R. Viotti, A. Vittone, M. Friedjung (eds.), Physics of formation of FeII lines outside LTE, Proc. IAU Coll. 94 (Capri), Reidel, Dordrecht, p. 217

Marmolino, C., Roberti, G., Vazquez, M., Severino, G., Wöhl, H. 1984, in E. Rolfe (ed.), Hydromagnetics of the Sun, Proc. Fourth European Meeting on Solar Physics, Noordwijkerhout, The Netherlands, ESA-SP220, p. 191

Marr, G. V., Creek, D. M. 1968, Proc. Roy. Soc. London, A 304, 233

Martin, W. C., Zalubas, R. 1981, J. Phys. Chem. Ref. Data, 10, 153

Mathisen, R. 1984, Oslo Inst. Theor. Astrophys. Publ. Series, 1, 1

De la Reza, R., Müller, E. A. 1975, Solar Phys., 43, 15

McKenna, S. J. 1984, Astrophys. Space Science, 106, 283

Moskvin, Y. V. 1963, Opt. Spectrosc., 15, 316

Omidvar, K. 1969, Phys. Rev., 188 nr. 1, 140

Omont, A. 1977, Journal de Physique, 38, 1343

Page, T. L. 1939, MNRAS, 99, 385

Pallé, P. L., Pérez Hernández, F., Roca-Cortés, T., Isaak, G. R. 1989a, A&A, 216, 253

Pallé, P., Régulo, C., Roca-Cortés, T. 1989b, A&A, 224, 253

Park, C. 1971, J. Quant. Spectrosc. Radiat. Transfer, 11, 7

Pierce, A. K., LoPresto, J. C. 1984, Solar Phys., 93, 155

Radzig, A. A., Smirnov, B. M. 1985, Reference Data on Atoms, Molecules and Ions, Springer Series in Chemical Physics 31, Springer, Berlin

Rhodes, E. J., Cacciani, A., Garneau, G., Misch, T., Progovac, D., Shieber, T., Tomczyk, S., Ulrich, R. K. 1988a, in R. C. Canfield, B. R. Dennis (eds.), MAX'91 Workshop #1, Summary and Reports, p. 33

Rhodes, E. J., Cacciani, A., Tomczyk, S., Ulrich, R. K. 1986, in D. O. Gough (ed.), Seismology of the Sun and Distant Stars, Proc. NATO Adv. Res. Workshop, Reidel, Dordrecht, p. 309

Rhodes, E. J., Woodard, M. F., Cacciani, A., Tomczyk, S., Korzennik, S. K., Ulrich, R. K. 1988b, ApJ, 326, 479

Robillot, J. M., Bocchia, R., Fossat, E., Grec, G. 1984, A&A, 137, 43

Roca-Cortes, T., Vazquez, M., Wöhl, H. 1983, Solar Phys., 88, 1

Roddier, F. 1965, Ann. d'Astrophys., 28, 463

Rothe, D. E. 1969, J. Quant. Spectrosc. Radiat. Transfer, 9, 49

Rutten, R. J., Kostik, R. I. 1982, A&A, 115, 104

Sandner, W., Gallagher, T. F., Safynia, K. A., Gounand, F. 1981, Phys. Review A, 23, 2732

Saraph, H. E. 1964, Proc. Phys. Soc., 83, 763

Scharmer, G. B., Carlsson, M. 1985, J. Comput. Phys., 59, 56

Seaton, M. J. 1951, Proc. Royal Soc. London Series A, 208, 418

Severino, G., Roberti, G., Marmolino, C., Gomez, M. T. 1986, Solar Phys., 104, 259

Shchukina, N. G. 1981, Astrometriya & Astrofiz., 45, 13

Shchukina, N. G. 1987, Kinematika Fiz. Nebesnykh Tel., 3, 40

Shchukina, N. G., Aleksandrova, I. I. 1982, Soln. Dannye Bull., 12, 100

Shchukina, N. G., Shcherbina, T. G., Rutten, R. J. 1990, in J.-O. Stenflo (ed.), Solar Photosphere: Structure, Convection and Magnetic Fields, IAU Symposium 138 (Kiev), Kluwer, Dordrecht, p. 29

Skumanich, A., Lites, B. W. 1985, in J. E. Beckman, L. Crivellari (eds.), Progress in Stellar Spectral Line Formation Theory, NATO ASI Series C 152, Reidel, Dordrecht, p. 175

Skumanich, A., Lites, B. W. 1986, ApJ, 310, 419

Snider, J. L. 1970, Solar Phys., 12, 352

Snider, J. L. 1972, Phys. Rev. Lett., 28, 853

Snider, J. L. 1974, Solar Phys., 36, 233

Snider, J. L. 1983, Solar Phys., 84, 377

Sobelman, I. I., Vainshtein, L. A., Yukov, E. A. 1981, Excitation of Atoms and Broadening of Specral Lines, Springer, Berlin

Steenbock, W., Holweger, H. 1984, A&A, 130, 319

Svanberg, S. 1971, Physica Scripta, 4, 275

Unsöld, A. 1955, Physik der Sternatmosphären, 2nd edition, Springer, Berlin

Vainstein, L. A., Sobelman, I. I. 1968, J. Quant. Spectrosc. Radiat. Transfer, 8, 1491

Vernazza, J. E., Avrett, E. H., Loeser, R. 1981, ApJS, 45, 635

von Uexküll, M., Kneer, F., Mattig, W. 1983, A&A, 123, 263

Waddell, J. 1962, ApJ, 136, 231

Weisheit, J. C., Dalgarno, A. 1971, Phys. Rev. Lett., 27, 701

Wiese, W. L., Smith, M. W., Miles, B. M. 1969, Atomic Transition Probabilities Volume II. Sodium through Calcium, NSRDS-NBS Ref. Data Ser. 22, Natl. Bur. Standards, Washington

Wijbenga, J. W., Zwaan, C. 1972, Solar Phys., 23, 265

Zimmerman, D. 1975, Z. Phys. A, 275, 5